

Optical/Infrared Signatures for Space-Based Remote Sensing

**R. H. Picard
E. M. Dewan
J. R. Winick
R. R. O'Neil**

Final Report

1 November 2007

APPROVED FOR PUBLIC RELEASE; DISTRIBUTION IS UNLIMITED.



**AIR FORCE RESEARCH LABORATORY
AIR FORCE MATERIEL COMMAND
Space Vehicles Directorate
29 Randolph Rd.
Hanscom AFB, MA 01731-3010**

REPORT DOCUMENTATION PAGE [example]				Form Approved OMB No. 0704-0188	
Public reporting burden for this collection of information is estimated to average 1 hour per response, including the time for reviewing instructions, searching existing data sources, gathering and maintaining the data needed, and completing and reviewing this collection of information. Send comments regarding this burden estimate or any other aspect of this collection of information, including suggestions for reducing this burden to Department of Defense, Washington Headquarters Services, Directorate for Information Operations and Reports (0704-0188), 1215 Jefferson Davis Highway, Suite 1204, Arlington, VA 22202-4302. Respondents should be aware that notwithstanding any other provision of law, no person shall be subject to any penalty for failing to comply with a collection of information if it does not display a currently valid OMB control number. PLEASE DO NOT RETURN YOUR FORM TO THE ABOVE ADDRESS.					
1. REPORT DATE (DD-MM-YYYY) 01-11-2007		2. REPORT TYPE Scientific Report - Final		3. DATES COVERED (From - To) 20-03-2000 to 30-09-2007	
4. TITLE AND SUBTITLE Optical/Infrared Signatures for Space-Based Remote Sensing				5a. CONTRACT NUMBER N/A	
				5b. GRANT NUMBER N/A	
				5c. PROGRAM ELEMENT NUMBER	
6. AUTHOR(S) R. H. Picard, E. M. Dewan, J. R. Winick, R. R. O'Neil				5d. PROJECT NUMBER 2301	
				5e. TASK NUMBER SB	
				5f. WORK UNIT NUMBER A1	
7. PERFORMING ORGANIZATION NAME(S) AND ADDRESS(ES) Battlespace Environment Division Air Force Research Laboratory 29 Randolph Road Hanscom AFB, MA 01731-3010				8. PERFORMING ORGANIZATION	
9. SPONSORING / MONITORING AGENCY NAME(S) AND ADDRESS(ES)				10. SPONSOR/MONITOR'S ACRONYM(S) AFRL/RVBYM	
				11. SPONSOR/MONITOR'S REPORT NUMBER(S) AFRL-RV-HA-TR-2008-1008	
12. DISTRIBUTION / AVAILABILITY STATEMENT Approved for Public Release; Distribution Unlimited.					
13. SUPPLEMENTARY NOTES					
14. ABSTRACT This report describes work carried out under the Air Force Research Laboratory's basic research task in optical remote-sensing signatures, entitled Optical / Infrared Signatures for Space-Based Remote Sensing. The work was carried out during the period 20 Mar 2000 - 30 Sep 2007 and was supported by funding from AFOSR's Physics and Electronics Directorate (AFOSR/NE). The objective of the program was to increase understanding of remotely sensed signatures, particularly as seen by spaceborne optical/infrared sensors. Emphasis was placed on understanding the radiance environment of the structured upper atmosphere of the earth (mesosphere and thermosphere) in terms of the structure of the underlying medium. Advances in non-LTE radiative transfer and atmospheric waves and localized excitations are detailed, as well as analysis and modeling of the databases resulting from two groundbreaking space infrared experiments, DoD MSX/SPIRIT III and NASA TIMED/SABER.					
15. SUBJECT TERMS Infrared, Radiative transfer, Non-LTE, Remote sensing, Retrieval, Gravity waves, Bores, Inversion layers, Turbulence					
16. SECURITY CLASSIFICATION OF:			17. LIMITATION OF ABSTRACT UNL	18. NUMBER OF PAGES 63	19a. NAME OF RESPONSIBLE PERSON R. H. Picard
a. REPORT UNCLASS	b. ABSTRACT UNCLASS	c. THIS PAGE UNCLASS			19b. TELEPHONE NUMBER (include area code)

Contents

PREFACE.....	vii
1. SUMMARY	1
2. INTRODUCTION	3
3. MIDCOURSE SPACE EXPERIMENT (MSX)	4
3.1. MSX Mission and Data.....	4
3.2. Atmospheric Gravity Waves.....	4
3.3. Auroras.....	7
3.4. Atmospheric Cooling Rates	9
4. TIMED/SABER.....	9
4.1. TIMED/SABER Mission and AF Contribution.....	9
4.2. Temperature and CO ₂ Mixing Ratio Retrieval	11
4.3. Tides.....	13
4.4. Temperature-Inversion Layers.....	14
4.5. CO ₂ 15- μ m Radiance Layers / "Knees"	16
4.6. NO 5.3- μ m Radiance	16
4.7. O ₃ 9.6- μ m Radiance.....	16
4.8. OH Layers, Interannual Variability, and Tracer Transport	17
4.9. Gravity Waves	19
4.10. Solar Storms.....	20
4.11. NO ⁺ (v) 4.3- μ m Emission, Thermospheric Temperature, and E-Region Solar Storm Response.....	21
4.12. Auroras.....	22
5. RADIANCE STRUCTURE.....	23
5.1. Localized structures	24
5.1.1. Temperature-Inversion Layers.....	25
5.1.2. Radiance Layers / Knees.....	25
5.1.3. Fronts / Mesospheric Bores and Ducted Waves	26
5.2. Wave and Other Structures	31
5.2.1. General.....	31
5.2.2. Atmospheric Gravity Waves, Sprites.....	31
5.2.3. Tides.....	34
5.2.4. Turbulence	34
6. RADIATIVE TRANSFER AND REMOTE SENSING	35
6.1. Radiative Transfer Methods.....	35
6.2. Radiative Transfer in Structured Atmospheres.....	36
6.3. Temperature and Species Profile Retrieval from Remote Sensing Data	36
6.4. Foliage-Canopy Radiative Transfer.....	37
6.5. Remote Sensing Meeting Organization	38
7. SPACE SURVEILLANCE	39
8. COLLABORATIONS	40
8.1. General.....	40
8.2. Support to Columbia Shuttle Accident Investigation	40
8.3. High Altitude Airship (HAA) and Near-Space Study	41

8.4. C/NOFS and Triggering of Spread-F.....	41
8.5. Satellite Drag	42
9. CONCLUSION.....	42
REFERENCES	43
PUBLICATIONS - 2000-2007	57
**Refereed	57
*Unrefereed	59
LIST OF ACRONYMS AND ABBREVIATIONS	63

Illustrations

Figure 1. MSX limb-radiance profiles taken 30 s apart in a view direction orthogonal to the velocity vector, showing considerable structure due to radiance layers in the 90-110 km region.	5
Figure 2. CO ₂ 15-mm cooling rates calculated from the three correspondingly colored scans of Figure 1 with the help of runs of the TIME-GCM model [Roble and Ridley, 1994], showing the large variation in cooling rate due to the presence of radiance layers.....	6
Figure 3. The northern polar region and locations of the MSX satellite and coordinating sensors on 9 February 1997 near 19:30 UT.	8
Figure 4. This panel shows the total AARC model radiance profile (red curve) for the 5-minute dosing case and its NO ⁺ (blue curve) and CO ₂ (green curve) components. The CO ₂ radiance profiles for dosing times of 1 and 3 minutes are also shown. The NO ⁺ emission is prompt and, hence, independent of the dosing history. The black curve is the MSX B2-band radiance profile.	9
Figure 5. TIMED satellite showing position of four instruments including SABER. SABER logo indicates cooperating entities including AFRL.....	10
Figure 6. Nighttime non-LTE T _k retrievals from SABER measurements on 3 March 2002 near 69N.	12
Figure 7. Compilation of SABER equatorial ascending/descending 15-μm radiance differences, corresponding to pairs of LTs separated by ~8.8 hours, for ten days spaced throughout a 33-day period in March-April, 2002.....	14
Figure 8. Percentage of all SABER scans in which at least one inversion layer exceeding 20 K was identified in retrieved T _k , as a function of latitude and LT for the Sep-Nov 2002 yaw cycle.	15
Figure 9. SABER nighttime OH 1.6-μm band mean-altitude statistics (left) and VER statistics (right) for the Jan-Mar 2006 yaw period.	19
Figure 10. Zonally-averaged GW-variance latitude-altitude cross sections for August 2003 from SABER and for August in two other years from the CRISTA-2 sensor on the Space Shuttle and the UARS/CLAES sensor.	20
Figure 11. NO 5.3-μm emission observed by SABER before the X18 solar X-ray flare of 28 Oct 2003 and after the flare at low latitude.....	22
Figure 12. OH Meinel CCD difference images (left) showing development of undular bore into turbulent, or foaming, bore over Ft. Collins, Colorado on the night of 6/7 Oct 2002 near 07:00	27
Figure 13. Solution of the BDO equation for the bore dimensionless stream function as a function of dimensionless horizontal distance X relative to a coordinate frame moving horizontally with the linear wave phase speed.	+..30

Figure 14. Illustration of the way the response of a "thick-screen" IR emitter varies according to the degree of alignment of the LOS with the wavefront.	32
Figure 15. Illustration of intermittence in high-resolution (10-m) wind profile data (left panel).	34

PREFACE

We gratefully acknowledge the support of Kent Miller of AFOSR in funding this work. We are also grateful for the many collaborations we have been the beneficiaries of in carrying out the effort. Most of our collaborators are cited in the text or appear as co-authors in the list of publications. We owe special thanks for the direct support of our colleagues at Arcon Corporation (Peter Wintersteiner, Edward Cohen, and Stanley Woolf) and at Boston College (Neil Grossbard).

Team member Edmond Dewan was awarded the 2002 Harold Brown Award by Secretary of the Air Force James Roche at the Pentagon on 20 May 2003. The Harold Brown award is unique in that it is presented for research that significantly increases the operational effectiveness of the AF. The award recognizes Dewan's work in developing the Dewan model for optical turbulent structure in the free atmosphere [*Dewan et al.*, 1993; *Dewan*, *2003, *2004]. The Dewan model depends on the realization that optical turbulence is a result of breaking gravity waves and exploits this dependence to predict the optical structure constant C_n^2 . This is discussed in Section 5.2.4 of this report. The model is being applied to developing an atmospheric decision aid for the ABL and to predicting seeing conditions at optical observatories such as Mauna Kea and the AFRL MSSS (Maui Space Surveillance Station) site on Haleakala. It may also be relevant to predicting small-scale structure that leads to background clutter for IR surveillance systems. The Harold Brown Award follows upon the receipt of the 2001 Guenther Loeser Memorial Award for Dewan's career scientific achievement in elucidating atmospheric and radiance structure. Dewan's Loeser Lecture, "On waves, spectra, and turbulence", was presented 9 Oct 2001. Previously, Dewan had won the Marcus O'Day Award for the best scientific paper of the year at AFRL/RV-East in an unprecedented two successive years (1999 and 2000). The award in 2000 was shared by team members Richard Picard and Robert O'Neil.

1. SUMMARY

This report describes work carried out under the Air Force Research Laboratory's basic research task in optical remote-sensing signatures, entitled Optical / Infrared Signatures for Space-Based Remote Sensing. This work was carried out during the period 20 Mar 2000 – 30 Sep 2007. It was supported by funding from AFOSR's Physics and Electronics Directorate (AFOSR/NE), in the portfolio of program manager Kent Miller.

The objective of the program was to increase understanding of remotely sensed signatures, particularly as seen by spaceborne optical/infrared (IR) sensors. Initially, the emphasis was on signatures of importance to missile defense, while later studies focused on signatures relevant for sensing resident space objects (RSOs) and related to space-weather applications. Much of the work focused on the environment of space objects and missiles, especially that constituting the mesosphere and lower thermosphere (MLT).

Much of the work carried out was based on two noteworthy satellite sensor databases. These are the unique but episodic data from the DoD MSX (Midcourse Space Experiment) satellite and the extensive global data from the NASA TIMED satellite. Both satellites carried advanced IR sensors in addition to other ultraviolet (UV) and other sensors. In the case of MSX, this was the SPIRIT III spectrometer and multichannel radiometer array, while TIMED bore the SABER multichannel radiometer into orbit. MSX, launched in 1996, has proven to be a rich source of information on a number of phenomena of importance, with the emphasis on atmospheric gravity waves (GWs) and on auroras during this reporting period. TIMED was launched in the second year of this effort, so the period of performance coincides quite nicely with the first six years of SABER data. TIMED/SABER research focused on (1) developing and validating retrieval algorithms, especially algorithms for retrieving temperature, pressure, and CO₂ volume mixing ratio (vmr), and (2) conducting science investigations based on the SABER data. The science investigations have included studies of temperature-inversion (TI) layers, tides, radiance layers, GWs, solar storms and auroras, and OH interannual variability.

The structure of the radiance environment is particularly important when one is seeking a space object, since it can reduce the detection probability and/or increase the probability of false alarm. Radiance structures can often be explained by understanding the structure of the underlying medium. A special emphasis was placed in this period on understanding localized structures of the MLT. These include vertically localized structures such as TI layers and horizontally localized structures such as fronts. One particularly important type of MLT front is the mesospheric bore, identified earlier by AFRL team members and studied further during the present period.

Progress was also made in the current period on the better studied forms of MLT structure, including atmospheric GWs, tides, and turbulence. One investigation observed and characterized concentric GWs and upward lightning from cloud tops known as sprites generated simultaneously by the same thunderstorm.

The ability to predict the radiative environment depends on a deep knowledge of radiative transfer. In the MLT region the atmosphere is never in local thermodynamic equilibrium (LTE). So radiative transfer becomes much more complicated, and non-LTE methods are required. Progress on non-LTE radiative-transfer methods occurred during

this period, especially methods for radiative transfer in structured atmospheres. This knowledge was applied to improving remote-sensing retrievals. Team members also collaborated as critics and reviewers with the authors of the first major book to be published on non-LTE atmospheric radiative transfer.

During this reporting period team members have participated in organizing an ongoing remote-sensing meeting and giving it a new focus on remote sensing of the middle and upper atmosphere. They also applied their knowledge of radiative transfer to coupling atmospheric and foliage-canopy radiative-transfer models in order to investigate possibilities for passive foliage penetration from a satellite sensor.

Toward the end of the period, studies began on exploiting ambient earth-atmosphere radiation to illuminate RSOs and on various methods to enhance detection and characterization of space objects.

The team has collaborated with a number of programs including the Columbia Space Shuttle Accident Investigation, the HAA program and the Near-Space Study, C/NOFS, and Maui MALT.

The work of the team was recognized by the granting of the Harold Brown Award to a team member by the Secretary of the Air Force and by the conferring of the Guenther Loeser Award and the Marcus O'Day Award to team members by the Battlespace Environment Division (AFRL/RVB).

2. INTRODUCTION

Much of the work in this task was focused on the environment of space objects and missiles, especially the MLT environment, with a special interest in a highly structured environment. The reason for this focus was that a structured environment can mimic a target of interest and be confused with it, resulting in a false alarm, or can act as unintentional camouflage enabling a target to hide, resulting in a missed detection.

The MLT region is at once the upper limit of the atmosphere and the lowermost region of space. As such, it is a transition region where a wholesale change of regimes takes place, including from turbulent to free molecular flow and from LTE to non-LTE radiative transfer. Energy is deposited by energetic solar radiation and by precipitating electrons and ions. Photochemical reactions and photochemical heating start to become very important, and the ionosphere starts to develop. As a consequence, free radicals and ions/electrons become significant species.

At the same time the region is notoriously difficult to study, both experimentally and theoretically. Since it is above the range of high-altitude balloons and aircraft and below the altitude where stable satellite orbits are possible, *in-situ* measurements can rarely be made there, and most of our knowledge of the region must come from remote sensing. Moreover, models are difficult because, as discussed above, virtually everything is important there and no effects can be neglected.

In order to address these issues we have developed an approach emphasizing collaboration with field and space experiments, data analysis, modeling, and theory. The approach was multi-pronged and involved a number of generic tasks, including the following:

- Investigate, specify, and exploit optical / IR spatiotemporal and spectral signatures for space-based remote sensing of space objects and their environment
- Construct first-principles models of phenomena contributing to important optical / IR signatures measured by existing instruments
- Extrapolate measurements using models from the measured parameter subspace to the total range of parameters of AF interest
- Validate models of optical / IR signatures by participation in satellite and ground-based field measurements
- Search for new phenomena to exploit and/or mitigate and new techniques applicable to increasing awareness of space objects and their environment.

We have expended much effort to analyze, understand, and model data from the pioneering MSX and TIMED space experiments, and have collaborated as well with ground-based observers and other analysts and modelers.

The results have been notable advances in knowledge of a number of aspects of remote-sensing signatures. We review these advances in the following sections. Sections 3 and 4 deal with the MSX and TIMED/SABER results, respectively. In Section 5 we discuss research in radiance structure and how it is related to the structure of the underlying medium, concentrating especially on localized structure. Research in radiative transfer and applications to remote sensing are discussed in Section 6. Section 7 treats preliminary research in surveillance of space objects. In Sections 8 and 9 we

discuss collaborations and conclusions. The report ends with references, a list of refereed and unrefereed publications under the task, and a list of acronyms and symbols. Further details of closely related work were described in *Donatelli et al. [2005].

3. MIDCOURSE SPACE EXPERIMENT (MSX)

3.1. MSX Mission and Data

The Midcourse Space Experiment (MSX) program was planned and implemented to support the design requirements for the next generation of space-based IR surveillance systems and to provide functional demonstrations of target detection against terrestrial, atmospheric, and celestial backgrounds. The satellite was launched on 24 April 1996 from Vandenberg AFB on a Delta II rocket into a nearly sun-synchronous orbit at an altitude of 900 km. As part of an extensive series of measurements, MSX successfully completed 150 episodic measurements, each nominally 20 to 30 minutes in duration, of IR atmospheric radiance and spatial structure in earthlimb scenes at tangent heights ranging from 30 to 150 km. The principal sensor onboard was the SPIRIT-III (Spatial Infrared Imaging Telescope III) radiometer and Michelson interferometer/spectrometer, developed by Utah State University's Space Dynamics Laboratory, which made measurements in a number of mid-wave IR (MWIR) and long-wave IR (LWIR) bands. The sensor suite also included the UVISI SPIMs (spectral imagers) and narrow-field and wide-field imagers, developed by Johns Hopkins University Applied Physics Laboratory and measuring from the visible into the ultraviolet (UV). IR measurements continued until the cryogenic supply of solid hydrogen was depleted on 25 February 1997. In one very productive type of experiment, high-resolution infrared images were recorded in a pushbroom scan mode by maintaining the SPIRIT III line-of-sight (LOS) at 90° to the LOS in the plane normal to the orbital plane. The MSX program objectives, sensors, and experiments are described further by *Mill et al. [1994]* and *O'Neil et al. [1994]*.

3.2. Atmospheric Gravity Waves

Efforts under this work unit dealing with GWs build on earlier pioneering papers by team members on observing GWs seen in the IR from earth orbit and modeling the process [*Dewan et al., 1998; Picard et al., 1998*]. The first paper analyzes two examples of circular concentric GWs seen in MSX B1-band (4.22-4.36 μm) below-the-horizon (BTH) near-limb scenes and shows that the waves are radiated from point sources associated with compact convective storms. The second paper calculates the spectrally resolved contribution functions (CFs) for CO₂(v₃) emission at 4.3 μm for various LOS, including ATH (above-the-horizon) and various BTH cases, both nadir and near-limb (sub-limb). By integrating over the B1 filter function, the paper shows that the MSX B1-band CF peaks near 45 km altitude and has no contribution from below the upper stratosphere. These and other MSX results on GWs were reviewed in *O'Neil et al. [1998]*.

Large spatial fluctuations and structure have been found in MSX CO₂ 15- μ m earthlimb data at tangent heights of 100-115 km (Figure 1). These fluctuations are not present in other bands such as CO₂ 4.3- μ m and have important implications for LWIR backgrounds as well as for the lower-thermospheric energy budget. The fluctuations are most likely due mostly to natural variations in the radiance layers, or "knees", occurring near 110-115 km (see Section 4.5), coupled with the passage of GWs. The implications for atmospheric cooling rates are especially significant (Figure 2), with substantial differences of up to 50K/d in the cooling rates associated with the three colored profiles of Figure 1 in the 100-km altitude region [**Picard et al., 2002*]¹. Radiance knees are discussed further in Sections 4.5 and 5.1.2.

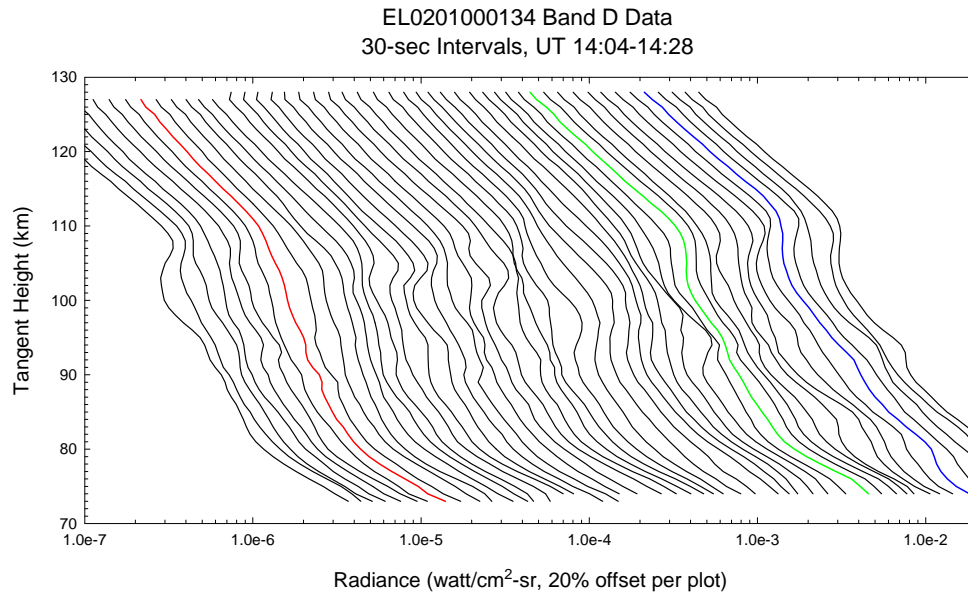


Figure 1. MSX limb-radiance profiles taken 30 s apart in a view direction orthogonal to the velocity vector, showing considerable structure due to radiance layers in the 90-110 km region.

The observed radiance from the MSX SPIRIT-3 radiometer contains spatial structure down to the scale of hundreds of meters. This spatial structure results from local fluctuations in the temperature and densities of the radiating states of the emitting molecular species, as well as fluctuations in radiation transport from the emitting regions to the observer. A portion of this database has been analyzed to obtain statistical parameters characterizing stochastic spatial structure in the observed radiance [**Brown et al., 2002*]. The analysis focused on five scenes in the CO₂ 4.3- μ m radiating region (4.22-4.36 μ m, MSX B1 band) and one scene in the atmospheric window region (6.8-10.8 μ m, MSX A band). The scenes included both ATH (limb) scenes and various BTH scenes,

¹ An asterisk (*) indicates an *unrefereed* publication by team members in the period of performance of this effort (2000-2007), while a double asterisk (**) indicates a *refereed* publication. The asterisks also label these publications in the list of References. Team-member publications are summarized in the Publications section, with subsections for **Refereed and *Unrefereed publications.

both nadir and near-limb (sub-limb). Using simple models, the observed statistics were shown to agree with prior observations and theoretical models of stochastic spatial structure generated by superposed and interacting GWs for special viewing geometries. The SHARC (Strategic High Altitude Radiance Code) model [Sundberg *et al.*, 1995] had been extended (SHARC 4) [Gruninger *et al.*, 1995, 1998, 2004] to predict the statistics of stochastic fluctuations in infrared radiance from the statistics characterizing temperature fluctuations in the middle and upper atmosphere for arbitrary viewing geometries. SHARC model predictions were compared with MSX data and shown to be in generally good agreement. Measured radiance power spectra were characterized by power laws over certain ranges of wavenumber which varied in a systematic way with nadir angle.

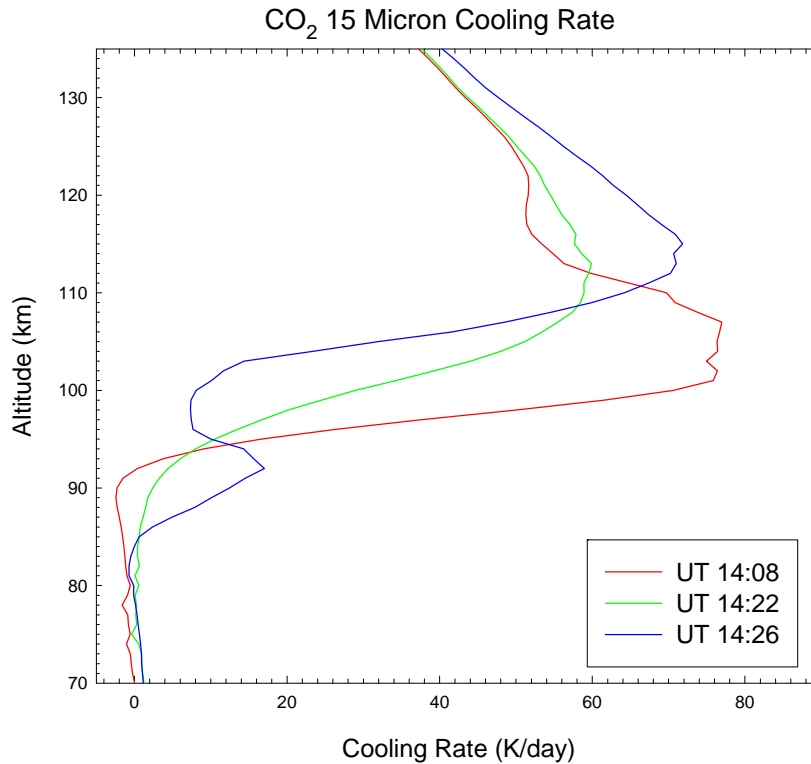


Figure 2. CO₂ 15- μ m cooling rates calculated from the three correspondingly colored scans of Figure 1 with the help of runs of the TIME-GCM model [Roble and Ridley, 1994], showing the large variation in cooling rate due to the presence of radiance layers.

Some of the IR radiance power spectra showed breakpoints where changes of power-law slope occurred. Both geophysical and observational explanations for breakpoints in the spectra originating from an atmosphere perturbed by superposed GWs were proposed [*Picard *et al.*, 2003a]. Previous works on the spectra of known sources of GWs and wave-filtering mechanisms by M. J. Alexander and others [Alexander, 1998; Pandya and Alexander, 1999; Piani *et al.*, 2000] and on the general expected characteristics of GW power spectra [Dewan, 1979, 1997; Cho and Lindborg, 2000] were reviewed. Then the

power spectra of LOS radiance fluctuations emitted and self-absorbed by an atmosphere perturbed by GWs were considered, including the shape of the spectrum and the spectral slopes. Examples of radiance spectra from gravity-wave-perturbed atmospheres that have two different slopes, with a steeper slope at large wavenumber, were analyzed, and possible mechanisms were discussed. The effect of latitude and season on the 4.3- μm fluctuations was also considered.

Although it is clear that explanation of radiance power-spectral breakpoints requires both geophysical and observational input, future research will be needed to complete understanding of their nature and properties. More emphasis will need to be placed on understanding spectra of orographically generated waves (mountain waves) and, in addition, the investigation will need to understand the behavior of higher moments, probability densities and exceedances.

3.3. Auroras

The MSX SPIRIT-3 radiometer window band, band A (6.8-10.8 μm) includes emission from rovibrational bands of CO_2 , H_2O , and O_3 . Under quiescent conditions, it does not include any emission from NO. The lower-thermospheric NO quiescent rovibrational airglow emission, largely excited by O collisions, occurs almost entirely in the first fundamental band (transition $v'=1 \rightarrow v''=0$). However, auroral electrons induce chemiluminescent reactions between $\text{N}(^2\text{D})$ or $\text{N}(^4\text{S})$ and O_2 , leading to production of higher states, $v' > 1$, in the fundamental band whose emission is transmitted in part by the band-A filter. On 10 Nov 1996, MSX saw enhanced emission in the A band at night between 110 and 130 km tangent height, and it was shown that the enhanced emission resulted from $\text{NO}(v)$ produced by strong auroral dosing [***Sharma et al.*, 2001]. Using the auroral electron energy flux, the location of the dosed region, and the MSX LOS, along with the N_2^+ First-Negative band emission at 391.4 nm measured onboard by the UVISI SPIMs, the 3-D energy deposition rate was derived. This rate was input to the SHARC auroral model [*Sundberg et al.*, 1995], which output radiance results in good agreement with MSX measurements.

A unique detailed study [***O'Neil et al.*, 2007] resulted from an auroral event observed on 9 Feb 1997 by MSX. The SPIRIT-3 radiometer on MSX observed enhanced 4.3- μm emission from a very well characterized aurora over the Barents Sea near 19:30UT, in conjunction with observations by the Polar and FAST satellites, the Loparskaya ground site, and the UVISI ultraviolet and visible spectrometers aboard MSX. The MSX track and the locations of the coordinated measurements are shown in Figure 3. Measurements of the auroral location, form, spatial extent, and dosing conditions were used to specify the component of auroral 4.3- μm radiance due to the time-delayed and optically thick CO_2 v_3 (00^01-00^00) radiation. An analysis based on the AARC (Auroral Atmospheric Radiance Code) IR auroral radiance model [*Winick et al.*, 1987] indicates: (1) the emission originates from near to and beyond the tangent point; (2) the optically thick CO_2 v_3 radiation is largely self-absorbed by the intervening atmosphere; and (3) the auroral enhancement is predominantly due to NO^+ $\Delta v = 1$ rovibrational transitions. In addition, the analysis indicates that the previously reported laboratory result for the NO^+ $v \geq 1$ vibrational yield from the reaction, $\text{N}^+ + \text{O}_2$ (reaction

1) is insufficient to account for the observed 4.3- μm emission. In order to explain the current results, we proposed that there is additional production from the reaction, $\text{N}_2^+ + \text{O}$ (reaction 2), forming $\text{NO}^+(\text{v})$ in vibrational levels $\text{v} = 0, 1$, and 2 with relative populations of approximately 0.25, 0.5 and 0.25, respectively. The AARC simulations for CO_2 alone and in combination with an NO^+ contribution are shown in Figure 4. The combined production processes yield an energetic electron-induced radiant efficiency of 0.56 ± 0.18 photons per auroral ion-pair for $\text{NO}^+ \Delta\text{v} = 1$ emission at altitudes equal to or greater than 112 km. This work enables the reliability of AF predictive models of auroral infrared radiance to be improved. In addition, it improves our knowledge of the auroral energy budget, where 4.3- μm emission plays a major role.

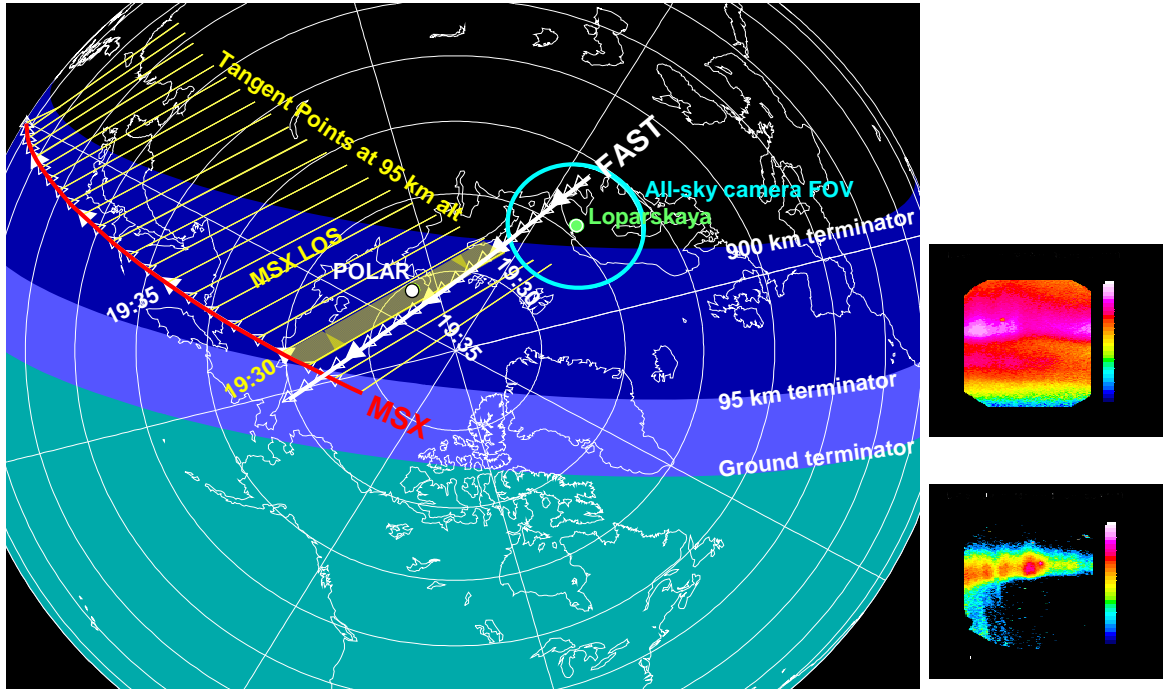


Figure 3. The northern polar region and locations of the MSX satellite and coordinating sensors on 9 February 1997 near 19:30 UT. The day-night terminator at 19:27 UT is indicated for altitudes of 0, 95 and 900 km and the orbital tracks of the MSX (red trace) and FAST (white) satellites are shown at selected times in the period from 19:25 to 19:48 UT. The end point of the LOS (yellow) of the MSX sensors is the location of the bore-sight tangent point at an altitude of 95 km. The nadir point of the Polar spacecraft and the 75° half-angle field-of-view (FOV) of the O(1D) all-sky camera at Loparskaya, projected to 250 km, are also shown. Beside the map are two images of the aurora from the MSX UVISI ultraviolet sensors at 19:29:14 UT. The top image is from the narrow-FOV imager, while the bottom one is from the wide-FOV imager.

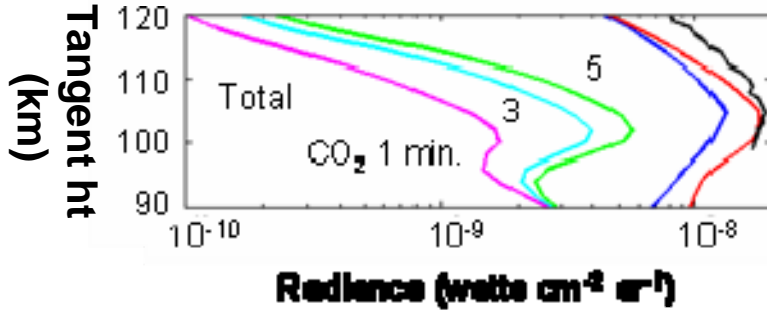


Figure 4. This panel shows the total AARC model radiance profile (red curve) for the 5-minute dosing case and its NO^+ (blue curve) and CO_2 (green curve) components. The CO_2 radiance profiles for dosing times of 1 and 3 minutes are also shown. The NO^+ emission is prompt and, hence, independent of the dosing history. The black curve is the MSX B2-band radiance profile.

3.4. Atmospheric Cooling Rates

Atmospheric radiative cooling rates, important for the atmospheric energy budget and dynamic models, have been inferred from MSX data [*Picard et al.*, 2002]. CO_2 15- μm emission is primarily responsible for cooling the atmosphere from the tropopause up to about 120 km. The cooling rates can become very large above 90 km, as shown in Figure 2. In addition, they are quite variable, depending a great deal on the structure, including the fine structure of the atmospheric temperature and species profiles.

4. TIMED/SABER

4.1. TIMED/SABER Mission and AF Contribution

The TIMED satellite [*Yee et al.*, 2003] is the first remote-sensing satellite ever designed to explore systematically the “ignorosphere”, the region between 60 and 180 km, above the range of *in situ* measurements by high-altitude balloons and below the range of *in situ* measurements by satellites in high-eccentricity orbits. SABER (Figure 5) [*Russell et al.*, 1999] is the main instrument (one of four) on TIMED and consists of a 100%-duty-cycle, ten-channel IR limb-scanning radiometer, measuring radiance bands from 1.27 μm [$\text{O}_2(^1\Delta_g, 0-0)$] to 15 μm [$\text{CO}_2(\nu_2)$] as a function of tangent height (Level 1 products). These radiance channels are inverted to yield retrieved atmospheric temperature, pressure, minor-species profiles, and radiative and chemical heating/cooling rate profiles (Level 2 products) as a function of altitude, as well as further more highly processed products. Typically, the altitude range is from 20 to 180 km or so, where the signal level reaches the noise. In some cases, such as NO under auroral conditions, the radiance data extends to considerably higher altitude (up to 300 km).

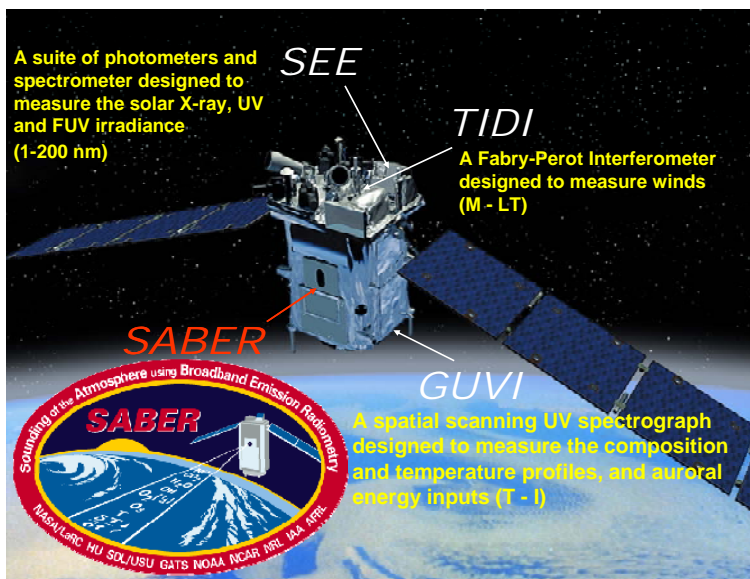


Figure 5. TIMED satellite showing position of four instruments including SABER. SABER logo indicates cooperating entities including AFRL.

TIMED was launched on 7 Dec 2001 from Vandenberg AFB into a near-circular 600-km orbit after many years of planning and of launch delays. It has been taking data since Jan 2002 and is now completing its sixth year of successful operation. The TIMED mission is managed by NASA Goddard Spaceflight Center and Johns Hopkins Applied Physics Laboratory, while NASA Langley Research Center and Hampton University manage SABER. The SABER instrument has operated with a 100% duty cycle since the inception of the mission and is still performing near-flawlessly. It was designed and fabricated by the Space Dynamics Laboratory of Utah State University.

Every one of the SABER channels is in the non-LTE regime over at least part of its altitude range. This is true for both the target species and some of the interfering species. Consequently, the retrieval process was a daunting task that had never before been attempted on this scale. An essential component of the retrieval codes is the non-LTE forward model that predicts the radiance from a specified atmosphere. In 1995 AFRL was asked to join the SABER Science Team because of its world-class expertise in non-LTE radiative transfer. AFRL personnel are regular participants in meetings of the SABER Science Team and also of the parent TIMED Science Working Group. See, for example, *Picard et al.* [2004].

Of particular relevance was AFRL's longtime experience with CO₂ non-LTE emissions. These include two SABER target bands--the ν_2 band at 15 μm and the ν_3 band at 4.3 μm —as well as the CO₂ laser bands at 9.4 μm , which are an important interfering emission in the SABER O₃ channel at 9.6 μm . AFRL team members have helped to design, test, and validate the innovative SABER retrieval algorithms (for example, *Mertens et al.* [2001]). SABER data is validated by comparison with models and with ground-based, airborne, and other space-based data. The latter include data from the old reliable NASA UARS/HALOE probe, from MSX, and from the new ENVISAT-1 / MIPAS probe launched by ESA in 2003. This AFRL involvement ensures the quality of the unique SABER data set and its availability and utility for AF purposes. It benefits especially AF models and codes of upper-atmospheric and space radiative structure. In addition, AFRL team members analyze data for significant effects,

dependencies, and trends. The collects to date have yielded remarkable data, increasing AF knowledge of the high-altitude radiative environment and of the underlying background atmosphere and its structure manifold. The database has gone through several versions, the current version being v1.06 with v1.07 soon to be released. The availability of global SABER retrievals of kinetic temperature (T_k), pressure, and mixing ratios of CO_2 as well as O_3 and H_2O on a 24/7 basis should improve model atmospheres such as SAG (SHARC Atmosphere Generator) [Adler-Golden, 1993] for DoD radiance codes. For the first time, SABER data organized by latitude, month, and time of day will provide a capability to the codes to characterize intrinsic variability. Specific examples of investigations involving AFRL personnel are in the following paragraphs.

4.2. Temperature and CO_2 Mixing Ratio Retrieval

The SABER temperature retrieval is critical, since most of the other retrievals depend on knowing the kinetic temperature, T_k , well. Also, the retrieval over the target altitude range (20-130 km) is a challenging retrieval that is in the non-LTE regime in the mesosphere and above and had never been attempted before. The retrieval uses the SABER CO_2 15- μm channel radiance to retrieve T_k . Pressure p is determined simultaneously with T_k by using both narrow-filter and wide-filter CO_2 channels according to the method of Gille and House [1971]. The retrieval uses two primary relaxation loops. In the inner loop, a T_k profile is retrieved using the top-down onion-peel approach, while pressure, CO_2 vmr, and the vibrational temperatures, T_{vib} , are held fixed. In the outer relaxation loop, the pressure profile is rebuilt from bottom up, starting at the lower boundary altitude using the onion-peel retrieved T_k profile and the barometric pressure law. The vibrational temperatures are updated using the CO_2 T_{vib} model with the previously retrieved T_k , CO_2 vmr, and pressure profile as input.

Originally, it was thought that CO_2 was uniformly mixed at least up to 90 km, so that, in the mesosphere, its vmr could be inserted *a priori* into the forward model to calculate temperature [**Mertens *et al.*, 2001]. This temperature profile could then be inserted into the CO_2 4.3- μm forward model to retrieve CO_2 vmr from SABER's 4.3- μm channel. However, it became clear through investigations carried out under the SABER program that CO_2 collisions were insufficient to keep CO_2 uniformly mixed and as a consequence CO_2 started to diffusively separate as low as 70 km altitude. This meant that T_k and CO_2 had to be retrieved *simultaneously* from the SABER 15- μm and 4.3- μm channels. An additional issue is that the production of $\text{CO}_2(\text{v}_2)$ states radiating at 15 μm depends on the atomic-oxygen concentration, and hence so does the retrieval of T_k above 90 km. There are several internal indirect limited methods of specifying [O] using SABER data, but there is no routine reliable [O] measurement onboard the TIMED satellite. Hence, one is often required to use climatological values of O, despite the fact that O is an extremely variable species whose variability is not inherently predictable, at least at the current time.

The basic $T_k - \text{CO}_2$ vmr joint-retrieval method has been documented in the literature [**Mertens *et al.*, 2003] and has been implemented in the SABER operational retrieval. The unique SABER temperature observations have been validated [**Mertens *et al.*, 2004] by comparison with rocketborne falling-sphere data from the summer MaCWAVE

Campaign [Goldberg and Fritts, 2004; Goldberg *et al.*, 2004; Fritts *et al.*, 2004] in Andøya, Norway in Jul 2002. Further validation efforts have used data from lidars at Table Mountain, Calif.; at Ft. Collins, Colo.; and in the Maui/MALT Campaign at the Maui Space Surveillance Site (MSSS), also known as the AMOS facility, on Haleakala, Maui, Hawaii, as well as satellite data from NASA's UARS/HALOE, and ESA's ENVISAT-1 / MIPAS probes. Examples of retrieved temperature profiles are compared to falling-sphere climatological data in Figure 6.

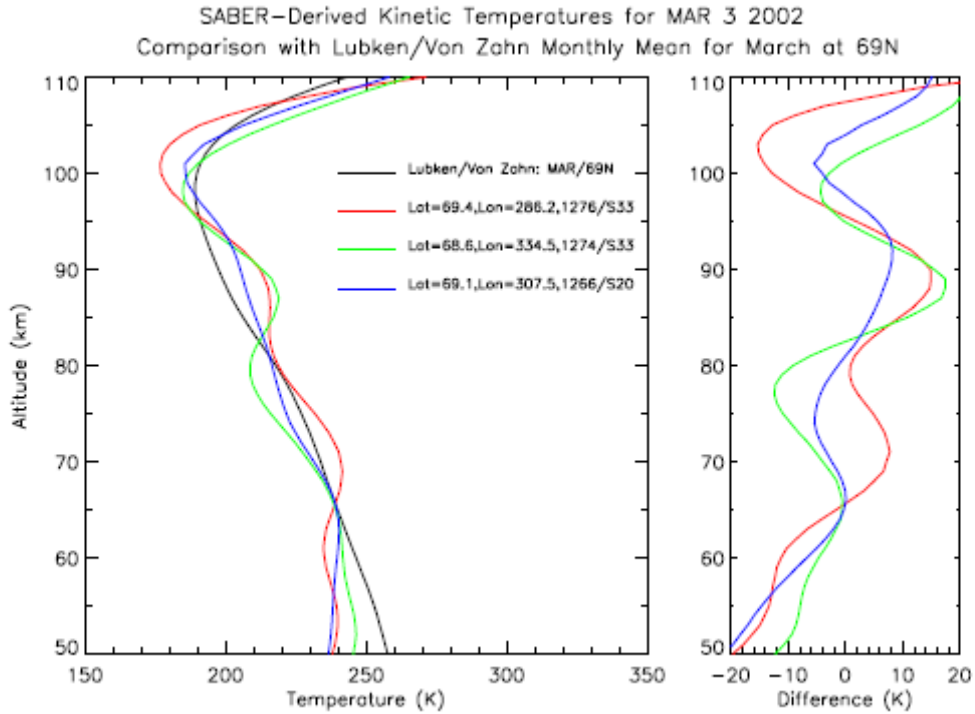


Figure 6. Nighttime non-LTE T_k retrievals from SABER measurements on 3 March 2002 near 69N. The latitude, longitude, orbit, and scan numbers, respectively, for the SABER measurements are indicated in the legend. The retrieved T_k profiles are compared to the climatological monthly mean March T_k profile from *Lübken and von Zahn* [1991] (black), and differences from the monthly mean are shown in the right panel.

Although SABER T_k values were generally in good agreement with independent measurements, an issue arose in the validation concerning the location of the polar summer mesopause and the value of its associated minimum temperature. In particular, it was noticed that the SABER mesopause was always up to 3 km lower in altitude and colder than the falling-sphere [Lübken, 1999] and lidar [Lübken and von Zahn, 1991] high-latitude summer measurements. One consequence was that noctilucent clouds would form at altitudes below 80 km, in disagreement with the results of ice-cloud microphysical models such as CARMA ([Rapp *et al.*, 2002] and references therein). This issue was addressed and solved [Kutepov *et al.*, 2006]. The main issue was that the SABER operational forward model lacked vibration-to-vibration (V-V) coupling terms involving redistribution of v_2 quanta among CO_2 isotopes. The AFRL team members collaborated in the investigation by carrying out a study of the effect of V-V coupling on

CO₂ v₂ vibrational temperatures (T_{vib}) in the polar summer mesopause region. This study involved runs of AFRL's ARC (Atmospheric Radiance Code) non-LTE radiance model [Wintersteiner *et al.*, 1992; Nebel *et al.*, 1994]. This study verified that proper treatment of the exchange of quanta between CO₂ isotopes lowers the summer polar mesopause T_{vib} for minor isotopes by as much as 25 K while increasing slightly the major-isotope T_{vib} . Because of this, the discrepancies between SABER retrievals and falling-sphere temperature measurements have been greatly reduced. Mesopause altitude is in better agreement, and retrieved conditions are now in accord with noctilucent-cloud observations.

Although analysis of SABER radiances for the CO₂ 4.3- μm and 15- μm bands have indicated that our non-LTE models are very good at predicting the daytime 4.3- μm radiance, there is a considerable underprediction at night. This is a longstanding problem for which the controversial Kumer mechanism [Kumer *et al.*, 1978] was proposed. The Kumer mechanism involves OH(v) vibrational energy transfer to N₂(v) and thence to CO₂ (V-V transfer). Since SABER measures two OH(v) $\Delta v=1$ bands along with the CO₂ bands, it is capable of resolving the issue of whether the Kumer mechanism is adequate or a new mechanism must be found. Evidence for an additional nighttime excitation mechanism for the 4.3- μm CO₂ emission in the mesopause region has been published [**Lopez-Puertas *et al.*, 2004]. A strong correlation was found between CO₂(v₃) 4.3- μm radiance structures near 85 km and the strength of the OH layer radiance in the 1.6- μm and 2.0- μm channels. Previous DoD experiments including ICECAP, SPIRE, and CIRIS-1A have noted similar correlations of CO₂(v₃) and OH(v) emission. Explaining the radiance requires that 2.8-3 N₂ vibrational quanta be created as a result of quenching one OH vibrational quantum by collision with N₂. This implies a fast, near-gas-kinetic rate for the V-V transfer, which may disagree with estimates based on chemical-kinetic arguments.

4.3. Tides

Signatures of the migrating diurnal tide (DT) have been identified in SABER CO₂ 15- μm equatorial radiance data. The migrating DT is forced by solar heating. Therefore, it is in synchrony with solar motion and hence also with local time. By separating data acquisitions into two halves centered on the ascending and descending nodes, respectively, yields data that is separated by approximately nine hours LT at the equator. Subtracting this data gives a strong DT signal at the equator that diminishes gradually as the latitude increases. A global map can be acquired in a single day. By accumulating such data for a full yaw cycle, during which the orbit precesses through all LTs (precession period ~ 65 d), the LT development of the tidal amplitude and phase can be determined [*Picard *et al.*, 2004]. The tidal signature is present in both the CO₂(v₂) 15- μm radiance and the retrieved temperature T_k . In Figure 7 we see an example of the tidal signal in T_k .

In the next two sections, we discuss the occurrence of temperature-inversion (TI) layers (Section 4.4) and 15- μm radiance layers or "knees" (Section 4.5), both of which turn out to be strongly connected with atmospheric tides.

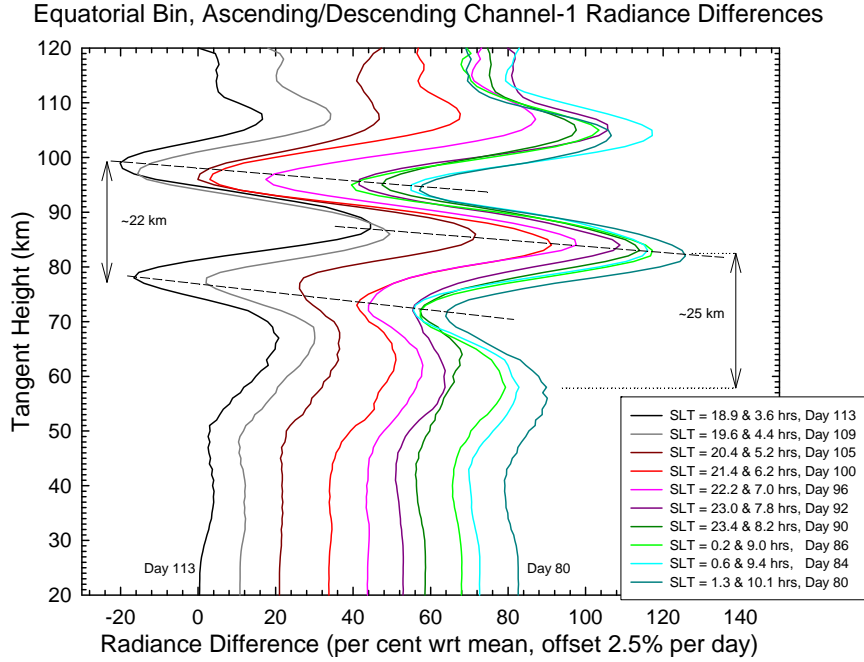


Figure 7. Compilation of SABER equatorial ascending/descending 15- μm radiance differences, corresponding to pairs of LTs separated by ~ 8.8 hours, for ten days spaced throughout a 33-day period in March-April 2002. The data are characterized by a vertical wavelength of 22-25 km, a growing amplitude with tangent height, and phase fronts descending with increasing LT at a rate of ~ 22 km/day---all characteristics of the diurnal tide.

4.4. Temperature-Inversion Layers

Earlier lidar work (see *Meriwether and Gerrard* [2004] for a review) had shown that TI layers are very common features of the mesosphere and mesopause region, which can be quite persistent and geographically extensive. The region above the TI has a small Brunt-Vaisala (BV) frequency N and thus a reduced static stability. This can also lead to a Richardson number, $Ri \equiv N^2 / \left[\left(\partial u / \partial x \right)^2 + \left(\partial v / \partial y \right)^2 \right]$, being less than $1/4$, where u and v are the horizontal wind components in the zonal (x) and longitudinal (y) directions. Hence, the region is dynamically unstable. The temperature lapse rate above the TI can even be superadiabatic, in which case the BV frequency is negative, the region is convectively (statically) unstable, and it will not support waves.

On the other hand, the inversion region below the temperature peak has a large BV frequency, is statically very stable, and can serve as a wave-duct region. For further details on ducted waves in TI layers, see Section 5.1 below. Earlier work by the authors has shown that TI layers likely arise from deposition of energy and momentum at a GW critical layer [*Huang et al.*, 1998]. The momentum deposition leads to accelerations of the background wind, which can result in large wind shears near the TI layer and further reduction of the Richardson number. For related work on TI layers, see Section 5.1.1. The first global study of temperature-inversion (TI) layers has been carried out under this task using SABER T_k data [*Picard et al.*, 2004]. Inversion layers are found to be globally common features of the MLT region, with amplitudes up to 90-100 K. The

amplitudes and widths of the layers and the altitudes at which the layers occur exhibit characteristic behavior as a function of season, latitude, and local time (LT). The latitude and LT dependence shows strong DT and semidiurnal tidal (SDT) signatures.

An example of binned occurrence probability distribution for the Sep-Nov 2002 yaw cycle is shown in Figure 8, using the Level 2A SABER data. The bins cover 2° in latitude and 1h in LT. There is no data near local noon since the sensor cannot look at the sun. Considering only inversions of at least 20 K, we find TI layers in 80-90% of all events in some regions of the latitude/LT space. If the threshold is reduced to 10 K, they are nearly ubiquitous in these same regions, which are mostly nighttime scans. On the other hand, in some other regions, the chances of seeing a large inversion are quite small. This is particularly true during daytime at high latitude and midlatitude. The DT dependence can be seen near the equator, while at northern midlatitudes there is a hint of developing SDT dependence. The tidal dependence is even clearer in the binned altitude distributions (not shown).

The large spatial extent of TI layers is also evident in the SABER data. Histograms of along-track length of TI layer regions show that TI layers are truly global features, often extending for 2000-4000 km and more along the tangent-point track.

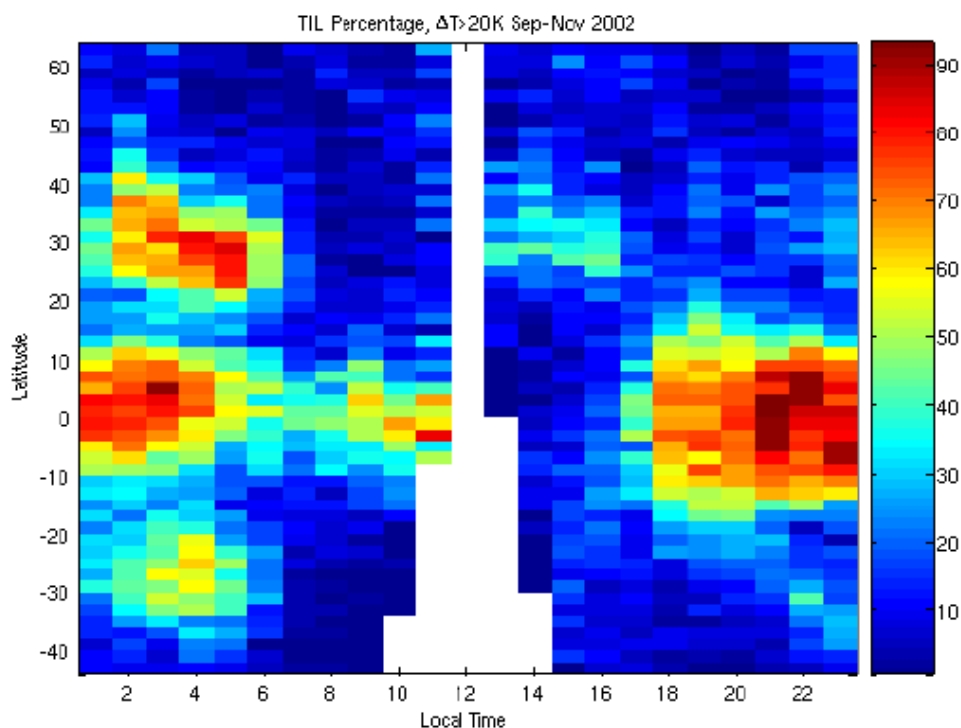


Figure 8. Percentage of all SABER scans in which at least one inversion layer exceeding 20 K was identified in retrieved T_k , as a function of latitude and LT for the Sep-Nov 2002 yaw cycle.

4.5. CO₂ 15- μ m Radiance Layers / "Knees"

There is always a change of slope in the CO₂ 15- μ m radiance near 110-115 km altitude. This change has been shown to be due to the onset of a new production mechanism for the CO₂(v_2) excited state, namely production by O collisions. Sometimes the change of slope is enough to produce a local maximum in radiance. These intriguing variable radiance layers or “knees” persistent in the 110-115 km altitude range have been characterized on a global scale using SABER data. They are also found to exhibit tidal signatures, but are not generally associated with TI layers. Standard radiance models using climatological atmospheric profiles are unable to predict reliably the occurrence of radiance layers. However, we have shown that radiance models incorporating DT modulation of the atmospheric profiles are capable of accounting—qualitatively at the present time—for the layer occurrence.

Atmospheric thermal tides from the GSWM (Global Scale Wave Model) [Hagan *et al.*, 1999; <http://web.hao.ucar.edu/public/research/tiso/gswm/gswm.html>] have been incorporated into the ARC non-LTE radiance model and the results used to determine the influence of tides on CO₂ 15- μ m radiance, with comparisons to SABER data. Although the resulting tidally driven model can account for the radiance knees, it is unable to account for the TI layers which are equally common features at lower altitude in the MLT region. By contrast, atmospheric climatologies, by themselves, without inclusion of the tidal effect in the radiative transfer, were unable to account for the radiance knees.

4.6. NO 5.3- μ m Radiance

Nighttime emissions at 5.3 μ m from nitric oxide (NO) measured by SABER were compared with the higher-resolution but more sporadic measurements from the MIPAS limb emission spectrometer on the European ENVISAT-1 probe. The vibrational, rotational, and spin temperatures were determined by fitting basis functions to MIPAS spectral data [Gardner *et al.*, 2007]. It was found that the NO 1-0 vibrational emission was in LTE below 110 km. Moreover, the rotational and spin temperatures converged near 110 km. Hence, NO rotational and/or spin temperatures can be used to estimate kinetic temperature T_k near 110 km. This is above the region where the standard SABER temperature retrieval from CO₂ 15- μ m emission is most reliable. These temperatures near 110 km were found to be considerably above temperatures from the NRLMSISE-00 model [Picone *et al.*, 2002], the standard semiempirical atmospheric model. The retrieval of NO($v=1$) and NO($v=0$) populations from the data were considered. The latter may lead to a useful retrieval capability, since most current retrievals (solar fluorescence or solar occultation) require sunlight and thus are restricted to daytime or terminator conditions.

4.7. O₃ 9.6- μ m Radiance

One method of ozone retrieval from SABER data uses the radiance from the SABER 9.6- μ m channel where O₃(v_3 , v_1) radiates. However, there are interfering emissions from CO₂(001-010) in this region, especially in daytime. These emissions are known as the CO₂ laser bands and arise from the same upper state that gives rise to the first

fundamental v_3 band of CO_2 . We have improved the existing model of the CO_2 v_3 -band emission by adding isotopic CO_2 V-V (vibration-to-vibration) coupling. This improved model has a number of useful applications. In particular, it was used to resolve discrepancies between the two different methods of retrieving ozone from the SABER data, the method from 9.6- μm ozone emission mentioned above and a method using the SABER 1.27- μm $\text{O}_2(^1\Delta_g)$ channel, by quantifying the interfering CO_2 laser-band emission in the 9.6- μm ozone-channel window. This study showed that the treatment of CO_2 bands was not the source of the ozone-retrieval discrepancies.

4.8. OH Layers, Interannual Variability, and Tracer Transport

OH Meinel-band rovibrational features arise from a chemiluminescent layer near 87 km altitude, primarily due to the reaction



They serve as an important probe of the mesopause region and dominate the quiescent nightglow. SABER measures the $\Delta v=2$ overtone Meinel emission in two bands, one near 1.6 μm from the low- v states ($v=1-3$) and one near 2.0 μm arising from the high- v states ($v=7-9$).

AFRL 6.1 team members have a long history of involvement with OH airglow modeling (for example, *Makhlouf et al.* [1995]) and participation in ground-based measurement campaigns, dating from the MAPSTAR, SOAR, and ALOHA programs [*Dewan*, 1994; *Makhlouf et al.*, 1998]. TIMED/SABER provides the opportunity to characterize the variability of OH Meinel emission on a global scale over a period of years.

The SABER OH Meinel-band data have been used to determine the global statistical characteristics of the OH layer's altitude, amplitude, and width as a function of latitude and LT. As an early finding from this analysis, OH double, and even triple, layers were found to be very common, contradicting the standard result that OH was distributed according to a simple Chapman-like layer. The occurrence probability of multiple layers was determined, and it was found that multiple layers occurred a very large fraction (as much as 40%) of the time. Double layers were reported previously by Melo *et al.* [2000] in analyzing UARS/WINDII data; however, the latter study found they only occur 5-25% of the time. Multiple OH-layer occurrence was found not to be correlated with the existence of large TI layers.

The reasons for the disagreement were investigated. We conjectured that the seeming prevalence of multiple layers could be spurious. Limb images of narrow layers or isolated objects are subject to inherent ambiguity as to where along the LOS structures giving rise to bright (or dark) features are located. SABER views the limb perpendicular to the orbit track, and uses a 1-D inversion of the limb radiance profile to retrieve volume emission rate (VER). The retrieval uses SABER's isolated slices through the limb, resulting in successive limb profiles about 1 minute or 400 km apart. At times this produces unrealistic profiles of OH VER, including peaks at 65 km (the photochemistry of OH does not allow for production of OH at 65 km at night), double peaks with a

secondary peak below 78 km, and negative OH VERs. Artifacts such as these can be produced by slight variation of the height of the profile along the LOS, caused by atmospheric GWs.

Work carried out with Edward (Ted) Llewellyn (Univ. Saskatchewan), PI for the OSIRIS instrument [Llewellyn *et al.*, 2004] on the Swedish Odin satellite, showed [Degenstein *et al.*, 2003] that, as suggested above, the assumption of a spherical-shell atmosphere implicit in the SABER (and WINDII) retrievals could lead to artifacts. The OSIRIS instrument makes tomographic measurements by scanning in nadir angle in the plane of the orbit and getting multiple views through a radiating volume. Thus it can distinguish structures in 2-D (altitude and earth-centered angle in the orbital plane). The atmosphere was perturbed with a GW having a horizontal wavelength of 200-400 km, a large vertical wavelength, and a vertical displacement of 1-2 km. The resulting limb radiance was calculated with the ARC model, and then the volume emission rate versus altitude was retrieved assuming a spherical-shell, horizontally uniform atmosphere. This process produced double-layer artifacts resembling some of the double layers in the SABER data. Consequently, the fractional occurrence of double layers is still an open question.

The SABER OH Meinel-band statistics have been calculated for the period 2002-2006, continuing into 2007. Interannual variability has been found in the altitude of the OH peak at high northern latitudes in winter. The high-latitude (70-80N) winter mesosphere is "normal" in 2002, 2003, and 2005, with an OH layer peak height of 87-88 km and an upper mesospheric temperature of 200-225 K. On the other hand, the mesosphere is anomalous in 2004 and 2006, with an unusually bright OH peak 5 km or more lower than the nominal normal 87-km height (81-82 km, and as low as 78 km) and an anomalously warm upper mesosphere of 260-280 K. The mesospheric anomalies are accompanied by anomalous stratospheric temperature and circulation, with an anomalously high stratopause altitude of 70-75 km [Siskind *et al.*, 2007]. Figure 9 shows the nighttime SABER OH 1.6- μ m band mean altitude and volume emission rate statistics for the Jan-Mar 2006 yaw period. The anomalously low bright winter OH layers are seen in the northern-hemisphere high latitudes.

These features can be explained by enhanced downward transport of odd oxygen caused by the unusual circulation. In the anomalous periods there is also enhanced downward transport of odd nitrogen (NO_x) into the stratosphere, which is important because it results in destruction of the ozone layer. Hence, the presence of very low and unusually bright OH layers in the mesopause region can serve as a warning, or even a proxy, for anomalously high NO_x and a hazard to the O_3 layer in the polar winter stratosphere.

The analysis of this data is continuing into 2007. The year 2007 is a normal year for the high-latitude winter mesosphere like 2003 and 2005. However, the variable behavior does not seem to be quasi-biennial in nature, since 2002 was also a normal year. Further correlations with stratospheric dynamics are underway. The anomalous OH layer behavior may turn out to be a leading indicator for winter-to-spring ozone destruction events brought about by the enhanced downward transport of NO_x . This work is being prepared for publication.

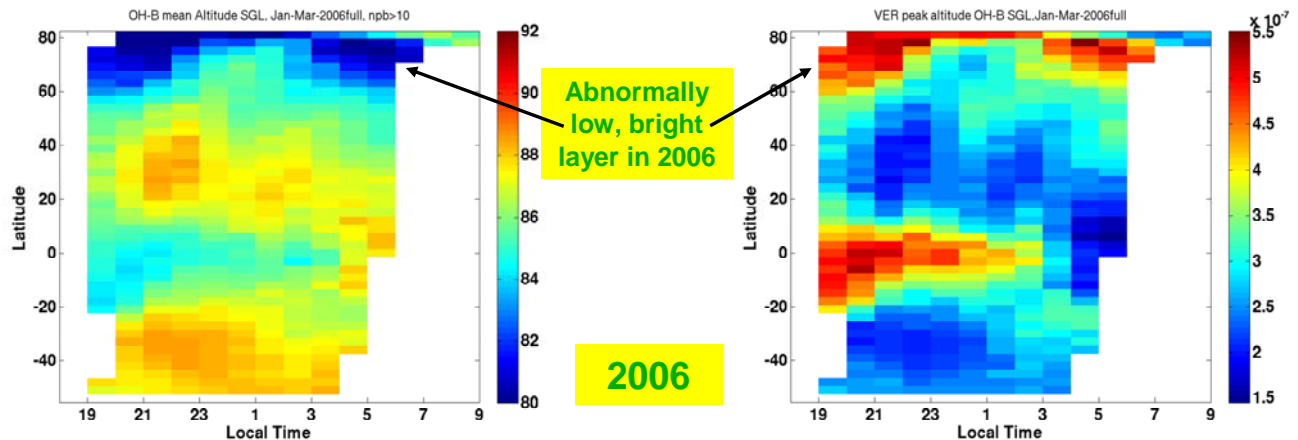


Figure 9. SABER nighttime OH 1.6- μm band mean-altitude statistics (left) and VER statistics (right) for the Jan-Mar 2006 yaw period.

4.9. Gravity Waves

SABER was not designed to monitor GWs. Yet, using the technique of *Fetzer and Gille* [1994], a residual method involving subtracting known zonal-mean, planetary-wave, and tidal perturbations from temperature variance data and identifying the remainder with the GW variance, temporally smoothed global GW variances can be extracted from a few consecutive days of data. The method was refined by Peter Preusse and collaborators [*Preusse et al.*, 2000, 2002] who applied it to Shuttle-based CRISTA 1 and 2 data. similar techniques were also applied by other researchers to UARS and EOS Aqua MLS data [*Wu*, 2001]. The method has now been used on SABER retrieved- T_k data, giving rise to global GW temperature-variance maps from 15 to 90 km altitude. Using SABER temperature variance data, the global characteristics of GWs have been determined [***Preusse et al.*, 2006]. The SABER data represent a major improvement in the altitude-range and temporal coverage using this method.

Global maps of GW variance at various altitudes and zonal-mean latitude/altitude cross sections were generated from SABER temperature data for Aug 2003 and compared to similar data from the CRISTA instrument on Space Shuttle for Aug 1997 and from the UARS/CLAES instrument for Aug 1993 (Figure 10). The data are in basic agreement and also were found to agree with runs of both the NRL GROGRAT GW ray-tracer and of the Warner-McIntyre spectral parametrization scheme, except in isolated features (underestimate of northern subtropical convectively generated waves and overestimate of northern high-latitude wave activity by the models).

The analysis for SABER has been extended to the first multi-year climatology of essentially continuous GW data spanning more than four years (2002-2006). The climatology shows a semiannual variation in the tropical upper stratosphere and mesosphere with peaks at solstices, along with strong wave activity in the winter polar region and weak activity near the summer pole. This data set has also been applied to the investigation of the quasi-biennial oscillation (QBO) and semiannual oscillation (SAO) in stratospheric and mesospheric waves.

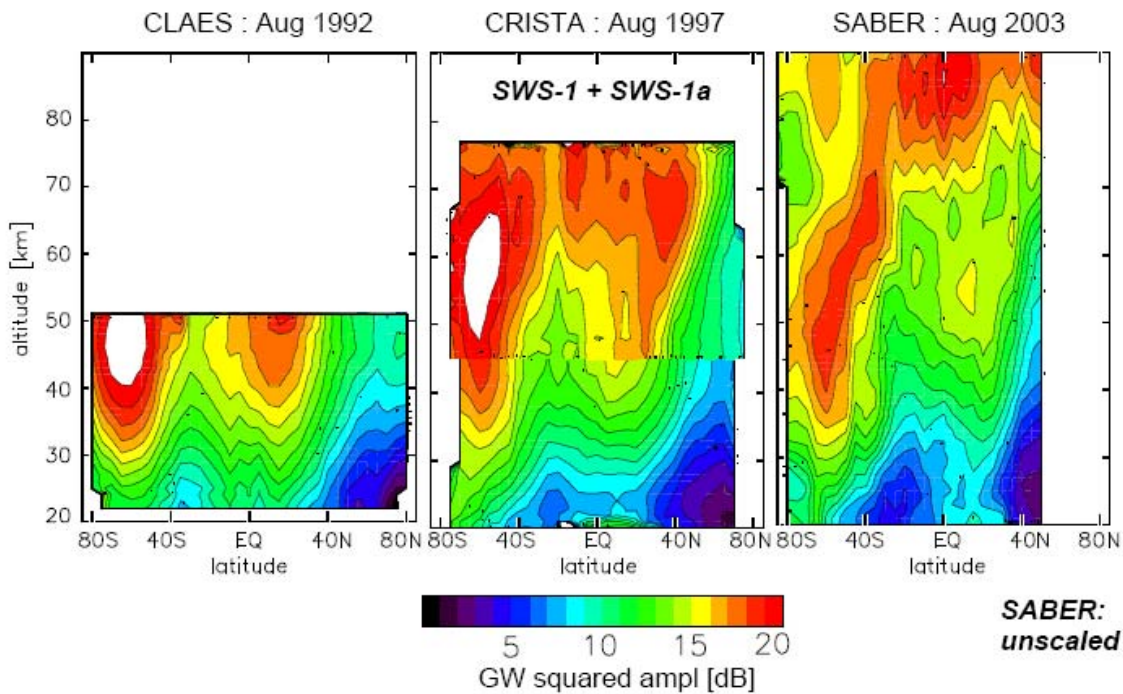


Figure 10. Zonally-averaged GW-variance latitude-altitude cross sections for August 2003 from SABER and for August in two other years from the CRISTA-2 sensor on the Space Shuttle and the UARS/CLAES sensor. The similarity of the plots stands out, as well as the superior altitude range of the SABER-derived data.

4.10. Solar Storms

Prior to TIMED/SABER, limited measurements of infrared response to auroral excitation existed. There were scattered sounding rocket measurements (for example [Stair *et al.*, 1975], a few measurements from CIRRIS-1A [Wise *et al.*, 1995], and a number from the SPIRIT-3 sensors on MSX [Sharma *et al.*, 2001; O'Neil *et al.*, 2007]. Although these earlier experiments provided information concerning the emitting species and helped validate models of the non-LTE mechanisms they gave little or no insight into the global nature of the response and the resulting effect on the thermospheric energy budget. SABER, with its virtually 100% duty cycle, has provided the first complete data and was fortunate to be observing during two major geomagnetic storm periods, April 2002 and October-November 2003 (the Halloween storm). The continuing unprecedented solar storms in the declining phase of the current solar cycle have provided extraordinary opportunities to document further the signatures of emissions from the disturbed atmosphere in the IR to UV spectral range.

Analysis of the response of the TIMED/SABER satellite IR channels to the intense solar-storm period in April 2002, coupled with observations of the entire sun-to-earth chain by approximately thirty other spacecraft, other sensors on TIMED including the GUVI uv sensors, and ground-based instruments, has yielded the most detailed knowledge to date of our understanding of the upper-atmospheric radiance response to

solar storms. AFRL 6.1 team personnel were involved in analyzing and understanding the wavelength channel dependence of the storm response. Detailed descriptions of energy transport in the Apr 2002 solar storm based on SABER data have been published [***Mlynchak et al.*, 2003; *Winick et al.*, *2004a, *2004b; ***Mlynchak et al.*, 2005], documenting the flow of energy into, out of, and within the thermosphere. To study the energy flow, the SABER data was enhanced by runs of the ASPEN thermospheric general circulation model. Enhancements of factors of thirty were observed in the SABER NO channel at 5.3 μm , accompanied by rich structure with strong latitudinal and longitudinal gradients. Auroral energy was transported into low latitudes and the equatorial region over a time scale of two to three days and was accompanied by sharp increases in low and mid- latitude radiance. This was followed by reestablishment of quiescent conditions over the course of a few days by a dramatic increase in the NO 5.3- μm cooling rate to ~ 2200 K/d, a negative-feedback, stabilizing process which we have called the “nitric oxide thermostat”. Reradiation by NO dissipated 50% of the energy input to the thermosphere by the Apr 2002 storm.

The team has also investigated storm effects in various other spectral channels. These include the CO₂ 4.3- μm band, the O₂(¹ Δ_g) 1.27- μm band, the OH 2.0- μm band, and, to a lesser extent, the OH 1.6- μm bands. Some of these bands, in particular 4.3- μm , show order-of-magnitude enhancements. The enhancement in the 4.3- μm channel is not entirely due to CO₂, but includes emission from aurorally enhanced NO⁺ ions, discussed further in the next section. The SABER 4.3- μm channel radiance enhancement maps show good correlation with similar maps of far-uv LBH (Lyman-Birge-Hopfield) band emission, clearly auroral, from the GUVI sensor onboard TIMED. Note, however, also that the solar-storm radiators in the OH channels are not related to OH. There has been some inconclusive investigation of the nature of these radiators; one strong candidate for the 2.0- μm channel is NO⁺-ion overtone emission.

In addition, the team investigated the response of SABER emissions to solar flares [**Winick et al.*, 2004b]. The flares are short-duration daytime events which affect all latitudes, even equatorial. Because of the TIMED orbit, it may take up to 12 hours for the SABER instrument to view the affected region. To minimize solar-wind (geomagnetic) effects, it is best to look at low magnetic latitude after a period of low geomagnetic activity (low Kp). The SABER data showed that there was a significant response of the NO 5.3- μm radiance to the historically large X18 solar X-ray flare of 28 Oct 2003, just before the intense Halloween solar storm. Figure 11 shows the clear response to the 28 Oct flare in the SABER 5.3- μm band radiance.

4.11. NO⁺(v) 4.3- μm Emission, Thermospheric Temperature, and E-Region Solar Storm Response

After identifying NO⁺ in auroral spectra from the rocketborne FWI experiment [*Picard et al.*, 1987], the AFRL team showed quantitatively, based on CIRRIS-1A data, that rovibrational emission from the NO⁺ ion is a significant contributor to radiance in the 4.3- μm channel under daytime or auroral conditions, in addition to the main CO₂ v₃ emission. This is significant for SABER since, as mentioned above, this channel is used to derive temperature and CO₂ vmr. Hence, solar storms or photoelectrons generated by

solar uv can enhance the emission in this channel and produce biases in the SABER temperatures, since T_k is retrieved in the SABER operational software ignoring NO^+ emission in the $4.3\text{-}\mu\text{m}$ channel. On the positive side, there is a potential for global measurements of $4.3\text{-}\mu\text{m}$ emission to give insight into E-region ion-neutral chemistry and energy transfer.

The response of the E-region to auroral electron dosing was investigated, based on global measured SABER nighttime $4.3\text{-}\mu\text{m}$ emission and SABER retrieved temperature, pressure, and CO_2 vmr [**Mertens *et al.*, 2007].

This study provides a unique perspective on E-region chemistry, energetics, radiative transfer, and response to solar geomagnetic storms. By modeling and subtracting the emission due to CO_2 from the measured $4.3\text{-}\mu\text{m}$ radiance, one is left with NO^+ emission, which can be related to E-region electron dosing through the FLIP model [Richards, 2002]. The SABER NO^+ VER was shown to be a useful proxy for the storm-time E-region response and will be used to develop parametrizations for storm-time corrections to the IRI (International Reference Ionosphere) [Bilitza, 2001] electron and ion densities. Analyses have been carried out for the April 2002 and Halloween 2003 storm periods. 6.1 team member Jeremy Winick and NASA Langley investigator Chris Mertens are continuing this work with partial funding from a NASA Office of Space Science Guest Investigator Grant.

For discussion of NO^+ emission in the MSX data, see Section 3.3 above.

4.12. Auroras

Possible auroral monitors internal to SABER data at 1.6 and $2.0\text{ }\mu\text{m}$ have been identified. The $2.0\text{-}\mu\text{m}$ auroral contribution is the stronger of the two. SABER was explicitly designed to avoid auroral emissions. However, these channels that were intended to monitor chemiluminescent OH Meinel-band emission at tangent heights of $83\text{-}96\text{ km}$ show a response at high-tangent heights $>100\text{ km}$ that is correlated with auroral energy deposition. This is particularly opportune since other TIMED instruments (GUVI

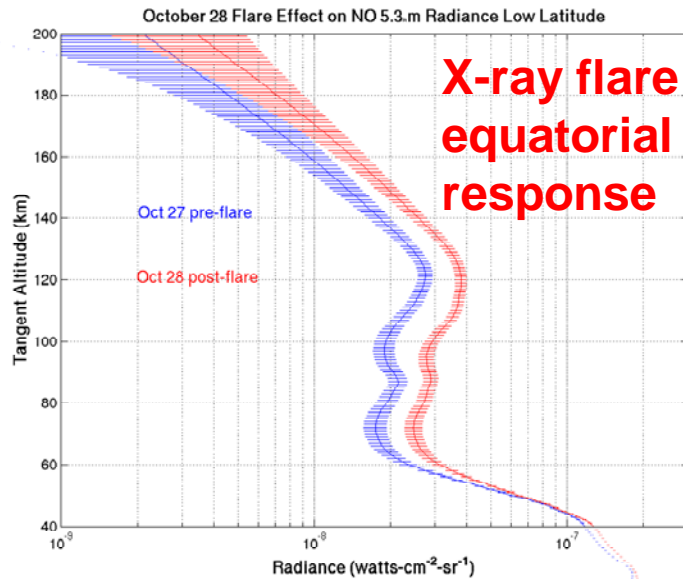


Figure 11. NO $5.3\text{-}\mu\text{m}$ emission observed by SABER before the X18 solar X-ray flare of 28 Oct 2003 and after the flare at low latitude. Each curve shows the zonal mean for the day, while the bars show the extent of the diurnal variation.

and TIDI) that could provide auroral inputs to SABER have proven to be less than ideal for this purpose, resulting in team members devoting considerable time to looking for internal auroral monitors. Work is continuing on identifying the source of the emission and its properties. Some candidates are NO^+ and possibly N_2^+ ionic emissions [*D. R. Smith, 2003]. The non-auroral background in these channels above 100 km tangent height is very small, since one is above the OH emission layer.

Other SABER spectral bands also respond to auroral dosing [*Winick *et al.*, 2004a], as discussed in Sections 4.10 and 4.11. (1) The NO 5.3- μm emission from the SABER 5.3- μm channel has an airglow component in the 1-0 band that is enhanced during aurora. In addition, there is copious production of hot fundamental-band emissions from NO during auroras [Winick *et al.*, 1987]. However, the fundamental auroral hot bands fall largely outside the SABER 5.3- μm channel bandpass. As discussed in Section 3.3, vibrationally excited NO is produced immediately by chemiluminescent reactions between $\text{N}(^2\text{D})$ and O_2 . This process will also enhance total NO. The NO produced could then be excited by atomic oxygen (the prime high-altitude quiescent $\text{NO}(v=1)$ production mechanism), leading to enhanced airglow and enhanced radiance in the SABER 5.3- μm channel. (2) The $\text{CO}_2(v_3)$ 4.3- μm emission has a strong nighttime quiescent contribution, but is enhanced in a strong aurora (IBC III or greater) [Stair *et al.*, 1975; Winick *et al.*, 1987]. The NO^+ rovibrational fundamental also radiates near 4.3 μm , and at night it is largely of auroral origin. Both the CO_2 and NO^+ emission will enhance the radiance in the SABER 4.3- μm bandpass during auroras. (3) Since the CO_2 laser bands at 9.4 and 10.4 μm also originate from the same v_3 upper state as the 4.3- μm emission, they are also enhanced. This will increase the amount of interference from CO_2 in the SABER O_3 9.6- μm channel. (4) The $\text{O}_2(^1\Delta_g)$ 1.27- μm band, which is measured by the shortest-wavelength SABER radiometer channel, is enhanced during aurora. This emission is most likely due to excitation of O_2 by auroral electrons.

We examined the correlation between the SABER channel and TIMED/GUVI LBH-2 channel radiance—a good proxy for the auroral dosing [*Winick *et al.*, 2004a]. It was found that the correlation was the strongest for the 2.0- μm channel, which appears to have a strongly linear response to dosing and the purest auroral response. On the other hand, the NO 5.3- μm channel correlation is the weakest, since there is a large quiescent component. In addition, the auroral response may be nonlinear and nonlocal, since NO is produced by auroras, has a long lifetime, and is advected by winds. The correlation of the SABER 4.3- μm channel with the GUVI LBH radiance is intermediate between the two above. Once again, there is a significant quiescent component. However, at higher dosing levels the airglow component is less important, there is less scatter, and a better linear correlation is established.

5. RADIANCE STRUCTURE

The nonequilibrium middle and upper atmosphere (30-160 km) are very dynamic regions that are structured vertically and horizontally by numerous processes. These include GWs, turbulence, fronts, layers, auroras, the terminator, thundercloud E fields, upward lightning (sprites and their kin), thermal plumes, and meteor trails. Of particular

interest is the passage of both atmospheric GWs and transient frontal disturbances or bores, as well as the presence of persistent TI layers. The infrared emissions from this part of the atmosphere, sometimes called the "ignorosphere", are not well characterized. They are typically not in LTE with the atmosphere and are further perturbed by the presence of the mentioned sources of pervasive atmospheric structure. The inevitable result is highly structured atmospheric emissions that depend on, but do not simply mirror, the structure of the atmosphere.

Understanding the structure of the atmosphere is essential to understanding the structure of the radiation that it emits. At the same time, understanding how atmospheric structure perturbs atmospheric radiation provides a means to sense the perturbing atmospheric processes remotely.

We have examined methods to calculate the LTE / non-LTE radiative response to temporal and spatial variations of the atmosphere and given examples of applications. Furthermore, we have compared our results with existing field data. In addition, we have found new phenomena in the underlying atmosphere (for example, undular bores), and more completely described known, but inadequately characterized, phenomena (for example, GW power spectra). We have studied the features and properties of these phenomena independently from the optical/IR radiation they emit, and, in many cases, we have also examined the resulting radiative structure. Further, the team has participated in the formulation of a proposed new and as yet unfunded NASA optical / infrared experiment (Waves Explorer), whose goal is to sense atmospheric GWs remotely from earth orbit on a global basis and characterize their sources. We discuss localized sources of structure in Section 5.1 and structuring by GWs and other phenomena in Section 5.2.

5.1. Localized structures

Atmospheric structures and the radiance structures they produce can be localized in the vertical direction, or in the horizontal direction, or both. TI layers are vertically localized structures having a strong effect on emitted and scattered radiation. These TI layers will typically be accompanied by radiance layers. In addition, in Sections 3.2 and 4.4 above, we have described radiance layers, or knees, that have a more complex origin and are not associated with TI layers. Temperature structure in general and TI layers in particular can produce GW-ducting regions. These ducting regions confine GWs and localize them in the vertical direction. Such wave ducts can also be formed by horizontal-wind curvature (Doppler ducting) [*Chimonas and Hines*, 1986] or by a combination of both temperature and wind structure [*Fritts and Yuan*, 1989].

Horizontally localized structures of importance include plumes, jets, and especially fronts. Fronts can involve primarily mass flow (gravity currents) or primarily phase motion (wave fronts) [*Simpson*, 1997]. In earlier work we discovered a new source of frontal disturbances in the MLT called internal-wave mesospheric undular bores. These wavefronts propagate in GW ducts and are seen as dramatic features of airglow imagery. Vertical localization due to layered radiating minor species is also possible. Such layers have been seen in the stratosphere in the form of narrow ozone laminae (for example, [*Reid and Vaughan*, 1993]). Other minor-species layers have been seen in tropospheric and stratospheric differential-absorption lidar profiles. This type of layering usually involves dynamical processes along with large gradients of minor-species vmr. The

MLT does have several common layered minor species, occurring in Chapman-like layers, whose layering is due to chemistry. Photochemistry results in layers that are quite broad, this layering is generally well understood. Examples are the Na and OH layers. However, to our knowledge, narrow minor-species layers of dynamical origin have not been reported in the MLT region, and we will not discuss them further. However, such layers, if present, would be expected to lead to enhanced radiance layers in a similar way to TI layers.

In Section 5.1.1 we discuss TI layers further. Section 5.1.2 deals with further comments on radiance layers, and Section 5.1.3 discusses mesospheric fronts, bores, and wave ducts.

5.1.1. Temperature-Inversion Layers

A case study on a mesospheric TI layer seen by the Univ. of Illinois sodium wind-temperature lidar in the NSF/AFRL ALOHA 93 Campaign at the AF MSSS site (AMOS) has been revisited [*Huang et al.*, 2002], showing conclusively that the TI layer resulted from GW critical-layer interaction. GW critical-layer interactions occur when the horizontal phase speed of the wave matches the background wind speed. When a critical layer occurs, the wave can interact with the background flow continuously and exchange energy with it. This can result in extraction of energy from the wave and acceleration of the background wind. The wind acceleration can lead to a region of large shear which is dynamically unstable ($Ri < 0.25$). In the resulting region of dynamic or shear instability, the wind shear produces turbulence and eventually heat, raising the temperature in a narrow TI layer.

The nature and source of these prevalent and persistent layers that provide stressing backgrounds for IR surveillance systems has been controversial. The original publication on the critical-layer mechanism for TI layers [*Huang et al.*, 1998], also involving team members, made the case for it, but used a less complete version of the ALOHA lidar data set in calculating the BV frequency. This showed the existence of dynamically unstable regions ($Ri < 1/4$). The reanalysis shows that there are also numerous regions of convective instability in the data, where N^2 is negative and $Ri < 0$. These regions also lead directly to turbulent heating. Thus both shear and convective instability play important roles in the TI layer development. The reanalysis explains new aspects of the observations, including the lack of local observation of the implicated GW in the MSSS CCD airglow imagery.

Satellite databases provide ideal opportunities to study TI layers on a global basis. A global analysis of the SABER data for TI layers is described in Section 4.4.

5.1.2. Radiance Layers / Knees

We have mentioned above that radiance layers, or knees, seem to have a complex origin. The striking layers in 15- μm CO₂ emission between 100 and 115 km can occur without the presence of any obvious TI layers. They appear to involve an elaborate interaction between atmospheric tides and radiative excitation/emission processes.

Unlike TI layers, such radiance structures are difficult or impossible to observe from the ground due to a combination of absorption by the lower atmosphere and foreground

path radiance resulting from lower-atmospheric emission. However, satellite remote-sensing databases, such as offered by MSX and SABER, are ideal tools for investigating the global behavior of radiance layers. The findings from MSX and SABER on radiance layers were discussed in Sections 3.2 and 4.5.

5.1.3. Fronts / Mesospheric Bores and Ducted Waves

A striking front covering the entire sky and followed by phase-locked waves was observed by ground-based CCD mesospheric-airglow imagers [Taylor *et al.*, 1995] taking part in the ALOHA 93 Campaign from the AMOS site on Haleakala. The front was dubbed the "Great Wall". When the sharp front was crossed, dramatic changes in radiance, either positive or negative, occurred. Such steps in radiance would result in stressing backgrounds for surveillance systems. AFRL scientists had explained the front [Dewan and Picard, 1998] as resulting from propagation of an undular bore in an internal-GW duct. Such bores are nonlinear propagating phase fronts and are well-known in many river estuary channels, as in the famous Bay of Fundy bore [<http://www.centralnovascotia.com/tides.php>] They have also been observed in oceanic internal waves [Osborne and Burch, 1980] and in waves on the atmospheric boundary layer. The latter include the so-called "morning glory" in the Gulf of Carpentaria, Australia [Smith, 1988] and the bores seen in the Central Plains in thunderstorm outflows [Doviak *et al.*, 1989]. Dewan and Picard [1998] adapted the existing theory for channel bores [Lighthill, 1978] to internal-wave bores by requiring that the internal bores possess a nodal line in the center of the duct. These so-called varicose modes result in geometrically symmetric patterns, while the resulting vertical displacements are described by antisymmetric functions. The nodal line plays the role of the rigid ground boundary in the channel bores. The sharp wave-structured fronts associated with mesospheric bores should lead to large gradients of background radiance seen by IR surveillance systems.

Subsequent to this work, a small explosion of activity in airglow studies of mesospheric bore and frontal propagation occurred. It was found that bores were infrequent, but not rare, events seen by many observers in all latitudes and seasons. Researchers have studied their occurrence characteristics at various geographically diverse sites. For examples, see [*Taylor *et al.*, 2003]. Surprisingly, according to some researchers, bores may occur as much as 10% of the time in the equatorial zone [Fechine *et al.*, 2005].

Natural questions that arise are what causes mesospheric bores and how are they generated. The first paper on the generation mechanism for mesospheric undular bores, was published by **Dewan and Picard [2001]. It was suggested that the body force required to generate the bore was provided by a GW exchanging momentum and energy with the atmosphere in a critical-layer interaction. As discussed in Section 5.1.1, GW critical-layer interactions were proposed [Huang *et al.*, 1998, **2002] as a mechanism for producing TI layers, which can provide regions of increased stability capable of ducting waves. **Dewan and Picard [2001] proposed that it is these very same critical-layer interactions that can launch bores. The body force generated at the critical-layer acts in piston-like fashion to produce a perturbation, which eventually becomes a bore by nonlinear steepening as the perturbation propagates through some distance. The method

of characteristics is used in this paper to predict the time required to form the bore, which is in agreement with data.

In an appendix this paper also enumerates the properties by which an airglow frontal observation can be identified as a mesospheric bore. The chief characteristic of note is the intensity step at the front. Such a sharp intensity step cannot arise out of linear GW interactions, since rectifying a non-zero-frequency GW requires that one be in the nonlinear wave propagation regime.

The first simultaneous and collocated observations of a mesopause-region undular bore and of the conjectured TI layer providing a duct for it were reported [***She et al.*, 2004]. The Colorado State Univ. (CSU) sodium wind-temperature lidar at Ft. Collins, Colorado made observations of the TI layer and the wind shift associated with the bore, while the CSU OH airglow CCD imager at Platteville observed the horizontal structure of the bore. Comparisons were made with the Dewan-Picard simple analytic bore model [*Dewan and Picard*, 1998, 2001], extended to include background wind. In this same publication the transition of an undular bore to a turbulent (or “foaming”) bore was observed for the first time (Figure 12). The bore must dissipate energy, but the foaming bore dissipates energy through its turbulent front rather than by shedding a short-period wave train. The foaming bore is more difficult to identify through airglow data than the undular bore because many observers routinely produce difference images (between successive frames) from their CCD airglow imagery, in order to enhance signal-to-noise ratio for wave perturbations. This means that the uniform background level change across the bore front will not be seen and the only identifying characteristic of the bore remaining will be a localized perturbation at the frontal boundary. The Richardson number Ri profile is calculated from the CSU lidar wind and temperature data, and it

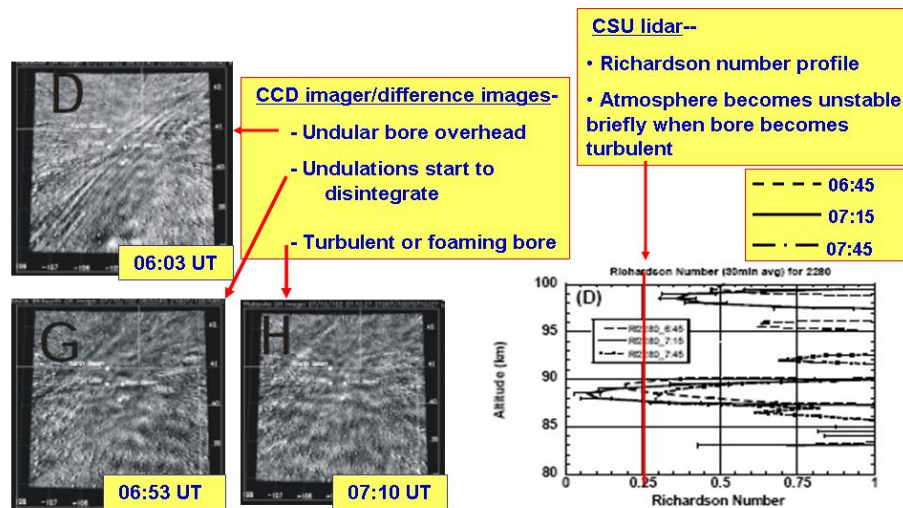


Figure 12. OH Meinel CCD difference images (left) showing development of undular bore into turbulent, or foaming, bore over Ft. Collins, Colorado on the night of 6/7 Oct 2002 near 07:00 UT. On the right the Richardson number Ri calculated from the CSU lidar wind and temperature data shows that Ri suddenly drops below 0.25 at OH emission altitudes simultaneously with the bore becoming turbulent.

shows

(Figure 12) that the atmosphere suddenly becomes dynamically unstable ($Ri < 1/4$) in the region of OH emission at the very time the undular-to-turbulent transition occurs.

In addition to the sharp front, the amplitude change across the front, the characteristic propagation speed, and the associated waves, the sense of the amplitude change across the front is significant. *Taylor et al.* [1995] were recording four airglow emission layers at the time of the ALOHA 93 bore. They found that the lower-altitude OH-Meinel and Na D-line emissions brightened as one crossed the front, corresponding to downward displacement of the air parcels, while the higher-altitude O(¹S) (or OI) green-line and O₂(¹Σ) Atmospheric-band emissions became less bright, corresponding to upward displacement. In the varicose-mode bore interpretation of *Dewan and Picard* [1998], this situation corresponds to a nodal line occurring between the Na and O₂ Atmospheric layers. We will call this a "normal" bore, since the nonlinear steepening that forms the bore can only occur if the displacement of the parcels as the bore passes is positive. This follows from the fact that the phase speed increases with amplitude. Negative bores, otherwise known as "inverse" bores, are not stable and will tend to flatten and disappear as they propagate.

A large database of two-color observations from Utah State University's Bear Lake Observatory has been searched for bores and related frontal phenomena [**Taylor et al.*, 2003]. These bores have been described, analyzed, and compared to bore theory. Many examples of normal bores were found. Some of these had complementary behavior of the low-altitude (OH) emission and the high-altitude (OI) emission, with a contrast reversal between the emissions, just like the ALOHA-93 bore. Others had no contrast reversal, with both emissions increasing in brightness across the front. In the varicose bore model, this corresponds to a nodal line occurring above both of the emitting layers. It was not long before observers found examples of "impossible" inverse bores. The CARI (Cornell All-sky Roving Imager) system found inverse bores in measurements at Arecibo, Puerto Rico on 6 Mar 1997 and at Colan-Piura, Peru on 24 Dec 2000. In these examples a bright front occurred in the high-altitude emission above a dark front in the low-altitude emission—apparently caused by a negative bore that is impossible according to bore theory. We suggested that this did not represent an observation of an inverse bore but rather indicated a dual bore, with one bore nodal plane above the higher airglow layer and the second below the lower layer [**Loughmiller et al.*, 2006]. The two bore responses are synchronized, but there is a horizontal phase lag in the upper-layer bore data consistent with the propagation time for an upward-propagating GW of appropriate wavelength between the two layers. This suggests that a common upward GW generated ducts for both waves. The ducts resulted from two TI layers formed by critical-layer interaction with a background wind modulated by the diurnal tide. The vertical wavelength of the tide is ~20 km which is greater than the separation of the two airglow layers in question, so the critical layers involved could have been formed by GW-tidal interactions at successive antinodes of the tidal horizontal velocity [**Loughmiller et al.*, 2006].

Observations of OH, sodium and atomic-oxygen green-line airglow at the AMOS site by the CASI (Cornell All-Sky Imager) instrument as part of the AFOSR-NSF Maui-MALT program were analyzed for the occurrence of bores [**Loughmiller et al.*, 2007]. Nine candidates were found in the period Jun 2002 – Jun 2003, including examples of

both normal bores and dual (inverse) bores. The imager data was correlated with SABER space-based temperature structure data from near-coincident limb scans. A number of TI layers were found in the SABER data, resulting in the presence of Brunt (thermal) wave ducts and corroborating the bore types seen in the imager.

On the theoretical front, progress has been made in developing a theory and numerical model for mesospheric undular bores that allows exploring the relations between such bores, nonlinear wave interactions, and solitons. The theory proposed by *Dewan and Picard* [1998], while extremely useful, contains numerous simplifying assumptions about the atmosphere and does not apply to general atmospheres nor permit detailed calculations. Moreover, it is not completely internally consistent [*Lighthill*, 1978, pg 466-467] and does not make connections with the larger body of nonlinear wave theory. On the other hand, the numerical model based on nonlinear wave theory (NWT) allows better understanding of the requirements for the existence of bores under more general conditions and better prediction of their occurrence. The NWT approach is less general than direct numerical simulation (DNS); however, its results are more easily interpreted than DNS results, since DNS is basically a numerical experiment and interpretation of its results requires the same degree of ingenuity as interpreting the results of an experiment. The NWT model was developed for the asymptotic long-wave regime and leads to clear interpretations within its range of validity. In the NWT the solutions factor and give rise to two coupled equations. These are the Taylor-Goldstein (TG) equation for the vertical behavior of the field and the Benjamin-Davis-Ono (BDO) nonlinear wave equation for the horizontal and temporal behavior in the deep-fluid case. The shallow-fluid case leads to a different nonlinear wave equation, the Korteweg-deVries (KdV) equation

Results from the NWT are currently being prepared for publication. These include the following: (1) Bores require a stable region in which to propagate. Unducted free waves cannot form bores. (2) The stable region required by bores does not necessarily require an inversion layer. Regions of wind curvature can also contribute to duct formation. NWT predicts bores can exist in Doppler ducts as well as in Brunt ducts formed by inversion layers. The basic requirement is that there be a region where the Scorer parameter is positive, bounded by regions of zero or negative Scorer parameter. (3) Only positive bores are stable. (4) The undulations behind the wavefront grow in number and increase in amplitude as the bore propagates. (5) The NWT shows clearly that the stability of bores results from balancing dispersion with nonlinear steepening. While infinitesimal-amplitude waves in a shallow fluid are dispersionless to lowest order, waves in a narrow waveguide (that is, a waveguide whose thickness is much less than the horizontal wavelength) embedded in a deep fluid are dispersive. (6) Small-amplitude bores travel at the linear long-wave phase speed c_0 , while large-amplitude bores travel at speeds greater than c_0 . (6) The waveforms of small-amplitude bores look like damped sinusoids, whereas those of large-amplitude bores are pulse-train-like and look distinctly cnoidal, with sharp crests and broad flat troughs. Individual pulses are starting to look like solitons. (7) The NWT equations support soliton solutions, where the balance of nonlinearity and dispersion is perfect. For the KdV equation, the solitons take the familiar sech^2 form, while the BDO solitons are algebraic Lorentzian functions. (8) Solution of the TG equation is an eigenvalue problem resulting in a set of modes for the duct characterized by an eigenvalue that is a function of c_0 . As the modal index is

increased, these modes have increasing numbers of vertical nodes and have decreasing phase speeds. The varicose mode of the Dewan-Picard model would be called mode 2 by the oceanographers, has a single node, and values of c_0 near 60 m/s. However, the NWT predicts a lower-order fast mode, mode 1, having no nodes in the vertical and c_0 near 180 m/s. This mode is described as sinuous rather than varicose, since the parcel displacements above and below the center of the duct are synchronized rather than being in opposition. Hence, it cannot lead to complimentary airglow emissions, regardless of the duct location relative to the airglow layers. (9) Addition of a Burgers term representing dissipation to the nonlinear wave equation can produce turbulent or foaming bores. As the coefficient of the Burgers term is turned up, undulations disappear and the frontal behavior becomes monotonic, while the front still maintains its sharpness. Sudden switching of the strength of the Burgers term will cause undular bores to evolve into foaming bores, or vice versa.

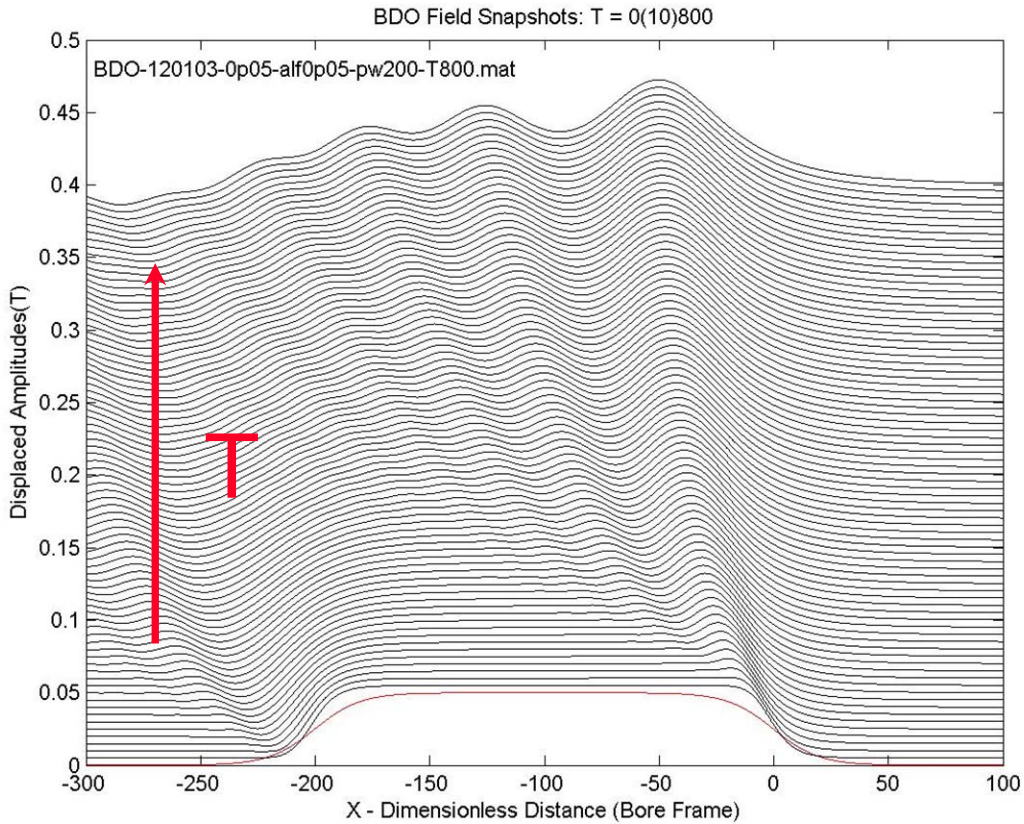


Figure 13. Solution of the BDO equation for the bore dimensionless stream function as a function of dimensionless horizontal distance X relative to a coordinate frame moving horizontally with the linear wave phase speed. The time development is shown starting from the initial value in red as a function of the dimensionless time T . The time increment is 10, with the solutions for successive times displaced upward by constant increments. The solutions are damped quasi-sinusoidal wave trains lengthening with time.

An example of solutions of the BDO equation in this model for small-amplitude initial values is shown in Figure 13.

5.2. Wave and Other Structures

5.2.1. General

The AFRL optical structure/signatures team has cooperated with the AFOSR/NSF Maui MALT program, which deployed an impressive array of sensors (CCD imagers, spectrometers, lidar, radar) at the AMOS site for a concerted attempt to characterize the sources of atmospheric structure. Participation in prior campaigns at AMOS (ALOHA 90, ALOHA 93) has been very successful and yielded valuable insights into the phenomena and mechanisms that lead to fluctuations in optical emissions. In addition, work with the MSX database has generated follow-on programs dealing with the emissions from wave-structured atmospheres.

Collaborations with field programs, including Maui MALT, and outgrowths of MSX investigations have led to a number of important results relevant to the structure of the atmosphere and the radiance it emits. Results on GWs are discussed in Section 5.2.2.

Thunderstorms are an important source of atmospheric GWs, and they also generate sprites (upward lightning from cloud top to space); simultaneous observations of GWs and sprites are treated in Section 5.2.2. Section 5.2.3 treats structuring by tides and Section 5.2.4 structuring by turbulence.

5.2.2. Atmospheric Gravity Waves, Sprites

The observation at 4.3 μm in an MSX BTH scene of a circular GW pattern radiating from a compact convective storm has been noted in Section 3.2. The angle of propagation seen in this pattern has been used [Dewan *et al.*, 1998] to infer the wave frequency or period and, with the measured horizontal wavelength, to infer the phase speed and the transit time from the source region to the region of observation. However, the MSX data can be used to infer further features of the waves. In particular, the contrast of the circular IR radiance pattern from unsaturated GWs generated by an isolated thunderstorm [Alexander and Picard, unpublished] depends on the angle between the sensor LOS and the GW phase front, maximizing when the LOS is aligned with the wavefront. This has been called the "Venetian-blind" effect and occurs because in the cases in question the CF is much wider than the GW wavelength along the LOS. (For the MSX SPIRIT III 4.3-mm B1 band, the width of the CF is 15-20 km, quite wide compared to typical airglow layer widths.) This information can be used to refine the estimate of wave characteristics and explains certain features of the observations. For example, it explains why only waves propagating toward the sensor and no waves propagating away from the sensor are observed. This effect is shown clearly in Figure 14.

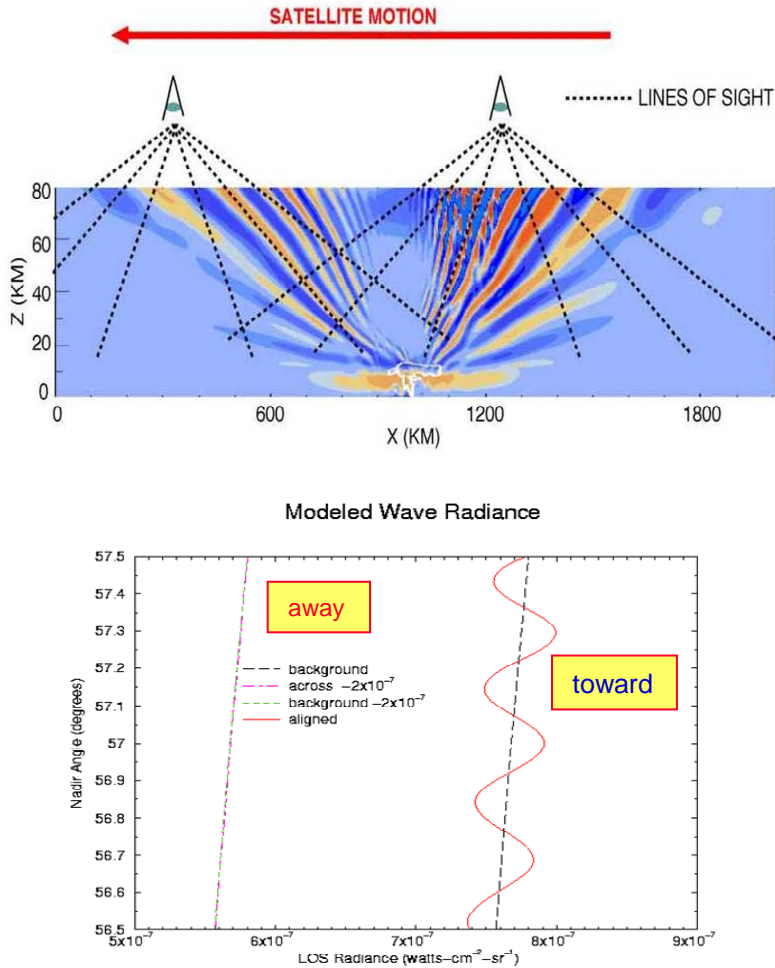


Figure 14. Illustration of the way the response of a "thick-screen" IR emitter varies according to the degree of alignment of the LOS with the wavefront. The top panel shows a thunderstorm-generated wave simulation (courtesy of M. J. Alexander) with several superposed LOS from a satellite-based sensor. The GWs are propagating outward and upward from the center of the storm. The bottom panel simulates the 4.3- μ m VER from MSX as a function of nadir angle over the 1° MSX FOV, centered on the angle where the LOS is aligned with the phase front. The simulation is run for an unperturbed atmosphere and for an atmosphere perturbed by a GW. The vertical (horizontal) wavelength of the wave is taken to be 10 km (32 km), and, for a sensor at the MSX orbital altitude of 900 km, perfect alignment will occur for a 57° nadir angle. The difference between the response to the perturbation when the LOS is aligned (GW propagates *toward* sensor) and when it is not aligned (GW propagates *away from* sensor) is clear.

On the basis of the MSX observations we received a NASA Office of Space Science grant (PI: Jeremy Winick; period of performance: Apr 2000 – Mar 2002) to develop techniques to sense gravity waves remotely using infrared emissions and airglow layers [**Picard et al., 2002*]. This work resulted in papers at several conferences and a NASA Office of Space Science report. One result from this work concerns techniques for doing rapid calculations of the atmospheric MWIR response to GWs. It was demonstrated that an approach to calculating the radiative response to GWs based on CFs for the

unperturbed atmosphere works quite well and cuts down enormously on computation time.

AFRL optical structure/signatures team members Jeremy Winick and Richard Picard have served on the Waves Explorer Science Team. Waves Explorer is a proposed \$180M MIDEX (mid-sized Explorer) satellite (PI: Gary Swenson, Univ. Illinois) that will carry out global gravity-wave surveys and will measure waves in the stratosphere using the 4.3- μ m IR technique pioneered by MSX. This mission has been proposed to NASA twice already (Aug 1998 and Oct 2001) without success. It may be proposed again if and when the opportunity arises, this time with David Fritts (Colorado Research Assoc.) as PI.

CCD imager observations of 715-920 nm emission from Bear Mtn., South Dakota in support of the NASA Sprites99 Balloon Campaign resulted in the first simultaneous observations from the ground of the sprites and GWs generated by a thunderstorm [***Sentman et al.*, 2003]. The GWs were seen in OH Meinel high overtones while the sprite emission resulted from the N₂ First-Negative fundamental and overtone band sequences. In addition, this was the first observation of the *complete* circular concentric ring pattern of a thunderstorm. We determined that this was possible because the GW vertical wavelength (~ 20 km) was much greater than the width of the emission layer (8 km). Thus there was no Venetian-blind effect. In the first observation of the concentric ring pattern from thunderstorm-generated waves [*Taylor and Hapgood*, 1988] and in the MSX MWIR observation from space [*Dewan et al.*, 1998], only partial circular patterns were observed because the vertical wavelength was too large. The total energy deposited by the sprites in the mesosphere during the Sprites99 Campaign observation was ~ 3.3 MJ, which is well below the level required to have a significant effect on the temperature in the OH emission region (~ 1 GJ). A video of the GW-sprite sequence is available. Several advances have been made in the description of GW power spectra. ***Dewan and Grossbard* [2000] showed that published balloon data on saturated gravity-wave power spectra, including several recently published papers, were contaminated by spectral leakage. This resulted in enhanced amplitude fluctuations and a coupling between spectral amplitude and slope, with resulting implications for the mechanisms responsible for the shape of saturated GW power spectra.

The linear saturation theory proposed by *Dewan and Good* [1986] to explain GW spectra was tested in a number of published works. *Allen and Vincent* [1995] used balloon-borne temperature data to test the model. They found that the data agreed well with the work of *S. A. Smith et al.* [1987], who had extended the Dewan-Good model, in the stratosphere, but did not agree in the troposphere. Dewan (unpublished, 2006) showed that the lack of agreement occurred because *S. A. Smith et al.* [1987] had used a separable power-spectral model, unlike the unseparable PSD in the saturated-cascade model of *Dewan* [1997]. When this assumption was eliminated and some additional considerations were applied, the disagreement between theory and data was eliminated. In addition to research on second moments of the saturated GW fluctuation amplitude (as typified by GW PSDs), important work was also carried out on properties of higher moments of the GW probability density function. A high-resolution study of stratospheric winds by smoke trails over scales where GWs are expected to dominate has shown, for the first time, that the saturated GW field is intermittent [**Dewan and Grossbard*, 2007]. The data is described by *Dewan et al.* [1984, 1988]. Figure 15

compares the smoke trail data with simulated data from a Gaussian random process. The difference is clear with the data showing large intermittence, while the Gaussian process is not (and cannot be) intermittent. A large "flatness" of the probability density function is taken as a quantitative measure of intermittence, where flatness is defined as the fourth central moment of the distribution divided by its variance squared. It is also shown that the rms shears are log-normally distributed. The theoretical interpretation of this behavior in terms of Dewan's saturated-cascade GW theory [Dewan, 1997] was compared to that arising from Lindborg's wave-free stratified turbulence cascade theory [Lindborg, 1999]. While neither approach was deemed to be completely satisfactory yet, the preponderance of evidence appeared to favor Dewan's saturated-cascade theory.

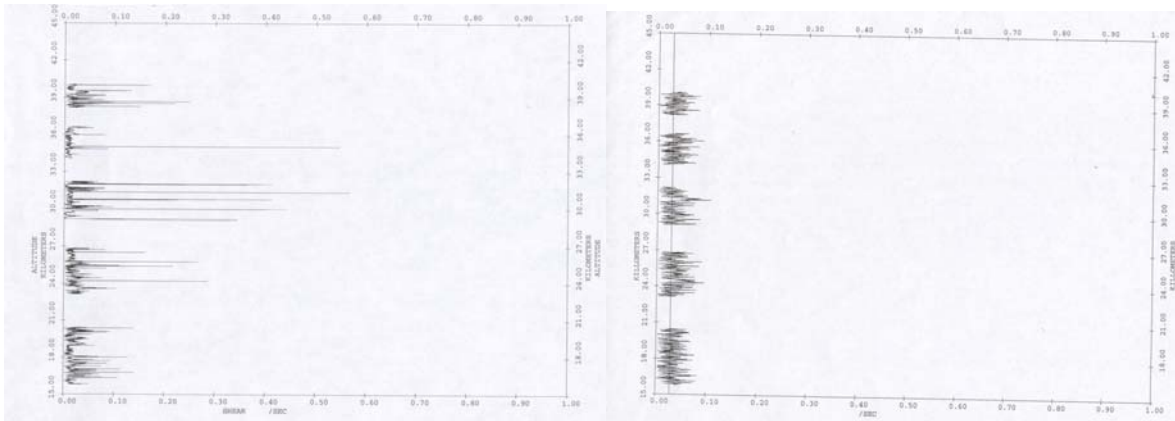


Figure 15. Illustration of intermittence in high-resolution (10-m) wind profile data (left panel). Data shown are vertical shears of total horizontal wind (s^{-1}), plotted from 15 to 45 km altitude. The right panel shows the shear for a simulated Gaussian random process wind profile for comparison. Both sets of shears have similar power spectra, but the tendency of the real data to stay near zero most of the time with sporadic very large excursions contrasts with the small but continuous excursions of the simulated data.

5.2.3. Tides

The ARC non-LTE radiative-transfer model has been modified to incorporate tidal modulation of the atmospheric temperature and density in the calculation of the 15- μm CO₂ ν_2 emission. This is necessary in order to model reliably the LT dependence of observed radiance structure. See the discussion in Sections 4.3 and 4.5 describing the occurrence of thermospheric radiance layers or “knees” in the SABER data and the comparison of the data to this model.

5.2.4. Turbulence

The role of turbulence in structuring light waves propagating in the free atmosphere has been addressed by Dewan *et al.* [1993]. The so-called Dewan model predicts the altitude profile of the optical refractive-index structure constant C_n^2 , which depends on high-spatial-resolution temperature measurements, on the basis of radiosonde data only, which have inherently low spatial resolution. This model has important application to

determining ground-based astronomical seeing [**Dewan, 2003*] and has resulted in an invention disclosure by Dewan *et al.* For this achievement, team member Edmond Dewan received the 2002 Harold Brown Award from the Secretary of the Air Force in May 2003.

In a recent publication [***Dewan and Grossbard, 2007*], it has been shown that a result of *Tatarski* [1971] relating C_n^2 to the outer scale of turbulence L_0 in the atmospheric boundary layer (ABL) severely underpredicts C_n^2 in the free atmosphere and must be modified. The reason for the underprediction involves the smaller-than-expected thickness of the turbulent layers and the minor fraction of the free atmosphere that is turbulent.

Turbulence fields are clearly intermittent. Recall also the results of Section 5.2.2, where GWs were also shown to be intermittent. Suppose it should happen that Lindborg's theory [*Lindborg, 1999*] cited there that interacting saturated GWs form a stratified turbulence cascade is correct. Then the range of spatial scales that can be considered turbulent will be extended considerably at the large-scale end, and the results on GW intermittence cited above could be considered results on the intermittence of (extended-range) turbulence.

6. RADIATIVE TRANSFER AND REMOTE SENSING

6.1. Radiative Transfer Methods

A detailed intercomparison of three different world-class 4.3- μm non-LTE radiative models and an operational non-LTE model has been carried out. These codes are the AFRL ARC line-by-line (LBL) radiative-transfer model [*Wintersteiner et al., 1992; Nebel et al., 1994*], the IAA (Instituto de Astrofísica de Andalucía) Curtis-matrix narrow-band model [*López-Puertas et al., 1986; López-Puertas and Taylor, 2001*], the hybrid SABER research model based on LINEPAK [*Gordley et al., 1994*] and developed by GATS (G & A Technical Software) and NASA Langley Research Center (LaRC), and the GATS/LaRC SABER operational non-LTE radiative code, based on BANDPAK [*Marshall et al., 1994*]. The agreement between the results obtained with these codes was remarkable, and any sources of discrepancy were isolated and identified. Since these codes have different heritage, were developed independently, and use independent and entirely different methods/algorithms, the agreement between them serves as evidence that the processes involved in this complex emission are well understood. This has resulted in confidence in the AF radiative codes and their ability to predict MWIR (mid-wave infrared) backgrounds. In earlier work [*López-Puertas et al., 1994*] the ARC and IAA non-LTE 15- μm models were compared, with similar good results.

LBL radiative-transfer methods are the most accurate methods for radiative transfer calculations. They are devoid of simplifying assumptions about the nature of the emission and free of the many pitfalls affecting band-model approaches. However, LBL calculations are notoriously time consuming. Methods for increasing the speed of non-LTE radiative models and generating rapid LBL radiative-transfer algorithms have been developed and implemented in the ARC model. These methods make possible otherwise unfeasible LBL calculations, enabling very rapid and accurate computation of vibrational

populations for different conditions. These acceleration methods depend on the use of stored functions to facilitate calculations and result in improved convergence and accuracy of the lambda-iteration technique used. We also found it important to correct properly for the assumption of homogeneous layers when considering optically thick bands. Using CO₂ emissions as an example, we have computed rapidly obtained radiance and cooling results that are useful to characterize the emissions from evolving and variable scenes. The algorithms were extended to time-varying situations, exemplified by auroras and have also been adapted to atmospheres perturbed by GWs, as discussed in Section 5.2.2.

Many improvements in the physics and photochemistry have been made in the ARC non-LTE LBL model for atmospheric CO₂ 4.3- μ m and 15- μ m emission, including addition of several V-V transfer processes. Note also the discussion in Section 4.2 of the addition of V-V coupling terms redistributing energy among CO₂ isotopes. As discussed there, addition of this process solved the problem of the discrepancies between SABER temperature retrievals in the summer polar mesopause region and data, and this change was kept as a permanent modification to ARC.

Finally, team members participated as consultants and evaluators in the formulation of the first book devoted to non-LTE radiative transfer in atmospheres. The book is entitled *Non-LTE Radiative Transfer in the Atmosphere*, and its authors are Manuel López-Puertas of IAA, Granada, Spain and Frederick W. Taylor of Oxford University. The book discusses AFRL models, in addition to treating AF and DoD space-based measurement programs in detail, starting with ICECAP [Stair *et al.*, 1975] and SPIRE [Stair *et al.*, 1985] and continuing through CIRRIS-1A and MSX. Participation by team members ensured that AF/DoD programs were properly represented and helped to assure the quality of the work.

6.2. Radiative Transfer in Structured Atmospheres

Our research in radiative transfer in structured atmospheres is discussed in Sections 3.2, 3.3, 4.5, 5.2.3, and 6.1. A review of some of this work has been published [*Picard *et al.*, 2002].

6.3. Temperature and Species Profile Retrieval from Remote Sensing Data

In the upper stratosphere and lower mesosphere, in daytime the CO₂ laser bands near 10 μ m (transition 00011 – 10001 in HITRAN [Rothman *et al.*, 2005] or Benedict notation) are populated by both LTE processes (thermal collisions) and non-LTE processes [solar fluorescent pumping, pumping by upwelling earthshine, energy transfer from N₂(v) excited by O(¹D)]. The high-resolution (~ 1 cm⁻¹) IR limb emission measured by the DoD CIRRIS-1A spectrometer flying on the Space Shuttle STS-39 clearly illustrates these effects. The presence of non-LTE emissions, if left unaccounted for, would seriously compromise the use of the laser-band emission to retrieve kinetic

temperature profiles. Since ozone radiates in this same spectral region, non-LTE emissions could also compromise the retrieval of ozone vmr from the data, particularly in the daytime. A non-LTE compensation technique was applied to the data whereby the non-LTE component of the radiance was modeled and subtracted from the total measured radiance [*Miller et al.*, 2000]. The kinetic-temperature profile and the O₃ vmr were then derived using the modified data. The correction for non-LTE used the ARC model [*Nebel et al.*, 1994] to calculate the CO₂ T_{vib} and FASCODE [*Smith et al.*, 1978; *Anderson et al.*, 1994] to compute the LOS radiative transfer. The LTE retrievals were then carried out on the residual radiance by Rodgers' optimal-estimation method [*Rodgers*, 1992; 2000] using FASCODE as the forward LTE-radiance model [*Miller et al.*, 1999]. The bands used in the retrievals were 940-960 cm⁻¹ (CO₂ laser-band P branch) and 789-794 cm⁻¹ (first laser hot band Q branch) for the temperature and 1073-1097 cm⁻¹ (O₃ ν₃) for the ozone vmr.

The SABER retrieval problem was alluded to earlier in Section 4.1. Every SABER channel possesses non-LTE radiators, either as the target species or as interfering species or both. A more fundamental approach to retrieval was necessary in this case, and the SABER retrievals, operational and otherwise, use a full non-LTE model for vibrational temperatures as an integral part of the forward radiative model. The full non-LTE forward model is used in a Rodgers-type optimal-estimation retrieval to do the inversion, similarly to the approach in the previous paragraph.

6.4. Foliage-Canopy Radiative Transfer

An atmospheric radiative-transfer code (MODTRAN 4) has been interfaced to a foliage-canopy model (LCM2) for the first time, enabling more accurate predictions of terrestrial sub-canopy structures seen from space [*Picard et al.*, 2001; *Ganapol et al.*, *2002, *2003]. The optical/infrared radiation emanating from the top of a foliage canopy contains spectral information, and perhaps also polarization and temporal information, about targets and human activity within and beneath the canopy, even when the foliage is totally obscuring. We have undertaken a modeling study to determine the extent to which this information may be recovered from hyperspectral imagery acquired by space-based sensors. Such passive methods hold the promise of considerable size, weight, cost, and power advantages over foliage-penetration radar. Using methods from radiative-transfer theory, we have found that the spectrally resolved upwelling radiance can indicate the presence and motion of a simulated target beneath a canopy under totally obscuring foliage, that is where the optical depth of the canopy is large or the leaf area index (LAI) ~5.

Using the LCM2 canopy code developed by collaborator Barry Ganapol of Univ. Arizona [*Ganapol et al.*, 1999], we have emphasized rapid exact analytic solutions of the equation of transfer based on the F_N (Facilitation-N) method [*Siewert et al.*, 1980]. More intensive discrete-ordinates or S_N methods (for example, *Evans and Marshak* [2005]) were also used along with computation acceleration techniques. LCM2 describes radiative transfer at two nested levels--within an individual leaf (LEAFMOD) as well as within a cloud of oriented leaves forming the canopy (CANMOD). LEAFMOD makes use of the specified absorption and scattering properties of leaves, while CANMOD uses the LAI and leaf-angle distribution (LAD) of the canopy as well as the output of

LEAFMOD. The lower boundary beneath the canopy is an absorptive/reflective surface simulating soil or a man-made target material.

The AF standard atmospheric radiative band model MODTRAN was used to describe the radiative transfer from the top of the canopy (TOC) to the satellite [Berk *et al.*, 1999, 2004]. We have focused on the solar reflective regime (0.4 - 2.5 μm), including the visible (VIS), near-infrared (NIR), and short-wave IR (SWIR), and have found considerable differences between the behavior in the VIS and the NIR range. Photons strike the TOC, are multiply scattered and absorbed in canopy, reflect from surfaces beneath canopy, traverse the canopy again with multiple scattering and absorption, and reemerge from the TOC. In so doing, they carry the spectral signature of elements in the canopy and targets beneath it. In the VIS region, the canopy is strongly absorptive and target signatures are weak. However, beyond the chlorophyll absorption edge, in the NIR and the SWIR, the absorption decreases dramatically, and a relatively large fraction of the photons incident on the canopy reemerge from the TOC and propagate to the spacecraft sensor imprinted with the signature of the target materials. This is true provided one avoids spectral regions where H_2O absorption bands of the canopy and atmosphere lie. The same is true in certain regions of the SWIR, once again avoiding water bands, although the incident solar radiance is declining fast here.

Under the SFFP (Summer Faculty Fellowship Program), LCM2 has now been extended to include a treatment of polarization [*Ganapol *et al.*, 2005]. Specular reflection has been introduced into the leaf scattering phase function in LCM2. Laboratory and field studies have demonstrated that the specular component of scatter from the leaf surface is the primary source of linear polarization in a canopy signal [Vanderbilt *et al.*, 1985a, 1985b]. So, first linear polarization was introduced, followed by progress toward a full vector theory of polarization.

6.5. Remote Sensing Meeting Organization

Team member Picard is principal Chair of the Conference on Remote Sensing of Clouds and the Atmosphere to be held as part of the SPIE Europe Remote Sensing and Security & Defence symposia in Cardiff, UK in Sep 2008. He has served as a Co-Chair and Program Committee member for the conference since 2001, introducing for the first time a focus on remote sensing of the middle and upper atmosphere to the conference. Other topics represented at the conference include radiative transfer and various other aspects of ground-based and space-based remote sensing. See, for example, Comerón *et al.* [2007] for the proceedings of the 2007 conference in Florence, Italy. Previous conferences were held in Brugge, Belgium (2006); Stockholm (2005); Gran Canaria, Spain (2004); Barcelona (2003); Agia Pelagia, Crete (2002); and Toulouse, France (2001). See the proceedings at Schafer *et al.* [*2003, *2004a, *2004b, *2005]. Participation in organizing the conference enables AF access to the international remote-sensing and structured-atmosphere research communities. The symposia address issues in the DoD and foreign defense communities, as well as NASA/ESA issues.

7. SPACE SURVEILLANCE

In the later years task activities have been expanded and reoriented in part to support remote sensing and signature studies of interest for space situational awareness (SSA) and space-object identification (SOI) applications. The purpose of this activity is to investigate the spatial, spectral, and temporal signatures characterizing RSOs.

We have considered space objects illuminated by non-conventional sources, including upwelling earth and earth-atmosphere radiation (earthshine and airglow). In addition to influencing the environment of RSOs and providing a source of radiance from which they must be distinguished, airglow and earthshine can illuminate RSOs in eclipse or during the dimmer lunar phases and at new moon. OH Meinel-band airglow is attractive as an illuminant because its radiance when integrated across all spectral bands is many mega-Rayleighs. See, for example, *Gruninger et al.* [2007]. Since its strongest bands are in the vibrational first-overtone region near 1.5 μm , a target region for optical fiber communications because of the fiber extinction minimum in that region, one should be able to take advantage of advances in NIR detector technology to make use of OH Meinel airglow more attractive. This approach is particularly appealing for objects in low earth orbit (LEO).

The OH airglow source has been implemented in the Optical Signatures Code (OSC). Although OSC was developed over an extended period by Teledyne Brown, the Army Missile Command, and predecessor organizations for missile-defense applications [www.teledynesolutions.com/docs/specsheets/0414_Optical_Signatures.pdf], it contains a lot of the functionality required for simulating the radiative signatures of space objects.

Because of the long optical path through a layer in the limb, the limb emission is most important in determining the RSO illumination. However, the limb enhancement peak is very narrow. On the other hand, the sub-limb (BTH) airglow comes from shorter paths but is associated with larger solid angles. An accurate model must take this subtlety into account. The full description of the problem is subject to the intrinsic diurnal, seasonal, latitudinal, and solar-cycle variability of the OH airglow, which is catalogued by SABER. The SABER database contains an extensive multi-year catalog of volume emission rates in two bright SWIR OH Meinel bands of interest for this application. As a result of the variability of the OH airglow, there can be significant variation of the upwelling radiance impinging on the RSO. One would expect the impinging radiance to vary as the RSO and the sub-RSO point move. This variation is due to a mixture of photochemical effects plus dynamical (tidal and other) effects. So a parametrized climatology of this variation from the SABER database may be of value.

When a ground-based sensor rather than a space sensor is viewing an eclipsed RSO, the use of airglow as an illuminant is much less attractive. This is because one must look through the airglow layer in the foreground, which will reduce the contrast of the RSO-reflected airglow against the background/foreground airglow.

Other airglow bands and earthshine bands from CO_2 , H_2O , NO , and other species radiating at wavelengths less than 2.5-3 μm can also be considered as illuminants. At longer wavelengths in the thermal regime, however, the atmosphere and the RSO become self-emitting, and an illuminant is so not useful.

We have also started to consider methods of RSO probing by using non-conventional methods. The latter include exploiting the information found in multipoint and multi-

time correlation functions. This leads to the consideration of interferometric methods (for example, *Monnier* [2003]), including both amplitude and intensity interferometry, for resolved and unresolved objects. Temporal interferometers, for example the prototype Michelson two-beam interferometer, have the potential to detect quite subtle temporal changes in targets, including those due to rotation, vibration, and relative motions. Spatial interferometers, such as the prototype Michelson stellar interferometer, can increase spatial resolution by effectively forming synthetic apertures. In addition, we have turned our attention more general techniques to enhance spatial resolution. Called generally superresolution techniques (for example, *Zalevsky and Mendlovic* [2004]), these methods seek to beat the so-called "diffraction limit" or the limitations imposed by the usual optical-system point-spread function.

8. COLLABORATIONS

8.1. General

Active collaborations have occurred with NASA (TIMED/SABER satellite, Waves Explorer satellite, MSX data exploitation and gravity-wave remote sensing) and with MDA (MSX modeling and analysis, radiative code enhancements for SBIRS). Collaborations have also occurred with NRO and the AF Warfighter hyperspectral imaging satellite program (foliage canopy and atmospheric radiative transfer), with the AFOSR/NSF Maui MALT program (gravity waves and localized structures), and with ESA (non-LTE radiative codes, ENVISAT 1 / MIPAS). These collaborations are generally treated in the preceding sections. This section ends with a discussion of a few collaborations not addressed above.

8.2. Support to Columbia Shuttle Accident Investigation

Team members Richard Picard and Edmond Dewan contributed to the investigation following the Columbia Space Shuttle accident in Feb 2003 on behalf of AFRL. Picard served on a distinguished panel of university and government experts investigating space/atmospheric environment effects on the Columbia accident and coordinated drafting of the panel's report [**Picard et al.*, 2003]. The panel was convened at the request of the NASA Johnson Space Center's Space Shuttle Vehicle Engineering Office, and its report concludes that an image that claimed to show a lightning bolt striking the reentering Columbia orbiter was the result of an artifact and that space/atmospheric environment effects by themselves were not responsible for the accident. Dewan provided a tutorial on weather in the mesospheric region of the atmosphere (50-85 km altitude) to the Columbia Accident Investigation Board at their request. This region can be subject to large temperature gradients and large wind shears, as well as ambient atmospheric electrical effects, and is critical to the reentering Shuttle orbiter, in this case representing the region where the orbiter broke up on reentry.

8.3. High Altitude Airship (HAA) and Near-Space Study

The potential hazards for high-altitude airships, such as envisioned in MDA's HAA program, and their systems due to upward lightning from cloud tops were assessed. The little-studied streamer discharges such as blue jets [Wescott *et al.*, 1995, 1998], blue starters [Wescott *et al.*, 1996], and the recently discovered gigantic jets [Pasko, 2003; Su *et al.*, 2003] are of particular interest as potential hazards. In addition, the potential for using such airships as platforms for investigating the emission from high-altitude discharges and other background sources was considered. Support was also provided to the AFSPC/AFRL Near-Space Study.

8.4. C/NOFS and Triggering of Spread-F

Exploratory studies were carried out relating to GW triggering of equatorial spread-F (ESF) by seeding the Rayleigh-Taylor instability [Hysell *et al.*, 1990; Huang *et al.*, 1993; Huang and Kelley, 1996a, 1996b, 1996c]. The occurrence statistics of spread-F suggests that it could be caused by GWs generated by convective storms [McClure *et al.*, 1998]. Since 200-km-scale structure is seen in radar backscatter [Hysell *et al.*, 1990; Huang *et al.*, 1993] and in the 630-nm airglow emitted by atomic oxygen from the perturbed F region thermosphere, this suggests that the horizontal wavelength λ_h of any triggering GWs should be ~ 200 km. Presuming that the triggering GW is generated in the troposphere and propagates linearly to the equatorial F region, then λ_h for the generated wave must also be ~ 200 km. For the wave to propagate to the F region without severe attenuation, the vertical wavelength λ_z must be large (~ 60 km). It follows from the GW dispersion relation that the period τ of the wave must be short (~ 15 min). Such waves do not appear to be generated by typical squall lines [Alexander *et al.*, 1995], but they can be generated by intense large long-lived thunderstorm complexes with cold high cloud tops (mesoscale convective complexes, or MCCs) that sometimes develop from squall lines [Vadas and Fritts, 2004].

As an alternative, if the Prakash mechanism [Prakash, 1999] is active then perhaps the triggering GW only needs to propagate to the extratropical E region, where it can induce a plasma excitation. The plasma wave then maps the excitation along the field line to the equatorial F region, triggering ESF. Waves having shorter λ_z can easily propagate to the E region. Thus, with this mechanism, waves generated by typical squall lines as well as by MCCs can both propagate to the E region and play a role in triggering spread-F. Notice, however, that even though GWs generally propagate obliquely upward, it is still true that one would expect a larger horizontal separation between the GW source region and the location of the spread-F in the case of the Prakash mechanism. Hence, the environment in which the GWs are generated and propagate can be quite different for the two mechanisms.

A procedure was also suggested for the TIMED spacecraft to investigate the influence of atmospheric GWs on ESF. The procedure makes use of data from two instruments on TIMED, specifically, SABER and GUVI. SABER data is used to look at GWs from 15 - 100 km altitude, as discussed in Section 4.9. The GUVI uv instrument can see spread-F on a global basis using the atomic-oxygen 135.6-nm emission. In the F region this signal

is due to radiative recombination of O^+ ions and thus is proportional to the electron density squared.

These investigations make use of team members' expertise in atmospheric GWs and support the goals of the C/NOFS program. It is expected that they will continue in the future.

8.5. Satellite Drag

SABER findings on thermosphere/mesosphere variability and structure were reviewed for the benefit of the satellite-drag research community. SABER's ability to retrieve remotely temperature and pressure profiles as a function of altitude on a global basis means that density profiles as a function of altitude are also known globally. Density is a critical parameter determining drag. These retrievals are routine through the mesopause and up to 100 km. Further extensions into the lower thermosphere up to the noise limit are also carried out, but are dependent on the proper retrieval or modeling of atomic oxygen.

9. CONCLUSION

This report describes a varied, rich, and productive research program carried out over an extended period in support of AF Space Situational Awareness (SSA) and Space-Object Identification (SOI) functions. Results have included significant advances based on the exploitation of space-based remotely sensed data, especially data from MSX and from TIMED/SABER. We have also extended the knowledge and utility of non-LTE radiative transfer, atmospheric GWs, inversion layers, bores, and turbulence. These advances have been recognized by the AF in the form of significant AF achievement awards. These advances indicate bright prospects for future impacts of related work on SSA and space-object detection/characterization.

REFERENCES

- Adler-Golden, S.M., *Description of the SHARC Atmosphere Generator*, Phillips Laboratory Technical Report, PL-TR-93-2123, 1993.
- Alexander, M. J., Interpretations of observed climatological patterns in stratospheric gravity wave variance, *J. Geophys. Res.*, *103*, 8627-8640, 1998.
- Alexander, M. J., J. R. Holton, and D. R. Durran, The gravity wave response above deep convection in a squall line simulation, *J. Atmos. Sci.*, *52*, 2312-2326, 1995.
- Anderson, G. P., J. Wang, M. L. Hoke, F. X. Kneizys, J. H. Chetwynd, L. S. Rothman, L. M. Kimball, R. A. McClatchey, E. P. Shettle, S. A. Clough, W. O. Gallery, L. W. Abreu, and J. E. A. Selby, History of one family of atmospheric radiative transfer codes, *Proc. SPIE*, *2309*, 170-183, 1994.
- Allen, S. J., and R. A. Vincent, Gravity wave activity in the lower atmosphere: Seasonal and latitudinal variations, *J. Geophys. Res.*, *100*(D1), 1327–1350, 1995.
- Berk, A., G. P. Anderson, P. K. Acharya, J. H. Chetwynd, L. S. Bernstein, E. P. Shettle, M. W. Matthew, and S. M. Adler-Golden, *MODTRAN4 User's Manual*, Tech Rpt, Air Force Research Laboratory, Hanscom AFB, Mass., 1999.
- Berk, A., T. W. Cooley, G. P. Anderson, P. K. Acharya, L. S. Bernstein, L. Muratov, J. Lee, M. Fox, S. M. Adler-Golden, J. H. Chetwynd, M. L. Hoke, R. B. Lockwood, J. A. Gardner, and P. E. Lewis, MODTRAN5: A reformulated atmospheric band model with auxiliary species and practical multiple scattering options, *Proc. SPIE*, *5571*, 78-85, 2004.
- Bilitza, D., International Reference Ionosphere, *Radio Sci.*, *36*(2), 261–265, 2001.
- *²Brown, J. H., R. R. O'Neil, R. H. Picard, W. A. M. Blumberg, E. M. Dewan, N. A. Grossbard, and J. H. Gruninger, Structure in middle and upper atmospheric infrared radiance, *Proc. SPIE*, *4539*, 431-445, 2002.
- Chimonas, G., and C. O. Hines, Doppler ducting of atmospheric gravity waves, *J. Geophys. Res.*, *91*, 1219-1230, 1986.
- Cho, J. Y. N., and E. Lindborg, Horizontal velocity structure functions in the upper troposphere and lower stratosphere 1. Observations, *J. Geophys. Res.*, *106*, 10223-10332, 2000.
- *Comerón, A., R. H. Picard, K. P. Schäfer, J. R. Slusser, and A. Amodeo, eds., *Remote Sensing of Clouds and the Atmosphere XII*, SPIE, Bellingham, Wash., 2007 [*Proc. SPIE*, Vol. 6745].

² An asterisk (*) indicates an *unrefereed* publication by team members in the period of performance of this effort (2000-2007), while a double asterisk (**) indicates a *refereed* publication.

- Degenstein, D. A., E. J. Llewellyn and N. D. Lloyd, The potential for incorrect interpretation of atmospheric images as seen with OSIRIS, *Sodankyla Geophysical Observatory Publications*, 92, 49-53, 2003.
- Dewan, E. M., Stratospheric wave spectra resembling turbulence, *Science*, 204, 832, 1979.
- Dewan, E. M., An investigation of the causes of optical and infrared airglow structures in the mesosphere, PL-TR-94-2261, Phillips Laboratory, Hanscom AFB, Mass., 1994.
- Dewan, E. M., Saturated cascade similitude theory of gravity wave spectra, *J. Geophys. Res.* 102, 29799-29817, 1997.
- *Dewan, E.M., *An Experimental Test to Compare Viability of Various Theories of Atmospheric Velocity Fluctuations*, Report AFRL-VS-TR-2001-1618, Air Force Research Laboratory, Hanscom AFB, Mass., 2001.
- *Dewan, E.M., Optical turbulence forecasting, *Proceedings Advanced Maui Optical and Space Surveillance Technologies (AMOS) Technical Conference*, 2003.
- *Dewan E.M., Modeling and forecasting atmospheric optical turbulence, *Technology Horizons*, Air Force Research Laboratory, Aug. 2004.
- Dewan, E. M., and R. E. Good, Saturation and the "universal" spectrum for vertical profiles of horizontal scalar winds in the atmosphere, *J. Geophys. Res.*, 91, 2742-2748, 1986.
- **Dewan, E. M., and N. Grossbard, Power spectral artifacts in published balloon data and implications regarding saturated gravity wave theories, *J. Geophys. Res.*, 105, 4667-4683, 2000.
- **Dewan, E. M., and N. Grossbard, The inertial range 'outer scale' and optical turbulence, *Envir. Fluid Mech*, 7, 383-396, Oct 2007a
- *Dewan, E. M., and N. Grossbard, Intermittence in stratospheric gravity wave cascades, submitted for publication (May 2007), 2007b.
- Dewan, E. M., and R. H. Picard, Mesospheric bores, *J. Geophys. Res.*, 103, 6295-6305, 1998.
- **Dewan, E. M., and R. H. Picard, On the origin of mesospheric bores, *J. Geophys. Res.* 106, 2921-2927, 16 Feb 2001.
- Dewan, E. M., N. Grossbard, A. Quesada, and R. E. Good, Spectral analysis of 10 m velocity profiles in the stratosphere, *Geophys. Res. Lett.*, 11, 80-83, 1984.
- Dewan, E. M., N. Grossbard, R. E. Good, and J. Brown, Power spectral densities of zonal and meridional winds in the stratosphere, *Phys. Scripta*, 37, 154-157, 1988.
- Dewan, E. M., R. E. Good, R. Beland, and J. Brown, *A Model for C_n^2 (Optical Turbulence) Profiles using Radiosonde Data*, Rpt PL-TR-93-2023, Phillips Laboratory, Hanscom AFB, Mass., 1993 [also available as NTIS: ADA-279-399].
- Dewan, E. M., R. H. Picard, R. R. O'Neil, H. A. B. Gardiner, J. Gibson, J.D. Mill, E. Richards, M. Kendra, and W. O. Gallery, "MSX satellite observations of

thunderstorm-generated gravity waves in mid-wave infrared images of the upper stratosphere,” *Geophys. Res. Lett.*, **25**, 939-942, 1998.

- *Donatelli, D. E., J. H. Brown, E. M. Dewan, J. J. Gibson, K. E. Kraemer, R. R. O’Neil, R. H. Picard, S. D. Price, R. D. Sharma, and J. R. Winick, *Background Clutter Specification and Mitigation*, Report AFRL-VS-HA-TR-2005-1107, Air Force Research Laboratory, Hanscom AFB, Mass. [limited distribution, U.S. Govt. and contractors], 29 Jul 2005.
- Doviak, R. J., K. W. Thomas, and D. R. Christie, A thunderstorm generated solitary wave observation compared with theory for nonlinear waves in a sheared atmosphere, *J. Atmos. Sci.*, **48**, 87-111, 1991.
- Evans, K. F., and A. Marshak, Numerical methods, in *3D Radiative Transfer in Cloudy Atmospheres*, edited by A. Marshak and A. B. Davis, Springer, Berlin, pp. 243-281, 2005.
- Fechine, J., A. F. Medeiros, R. A. Buriti, H. Takahashi, and D. Gobbi, Mesospheric bore events in the equatorial middle atmosphere, *J. Atmos. Solar-Terr. Phys.*, **67**, 1774-1778, 2005.
- Fetzer, E. J., and J. C. Gille, Gravity wave variances in LIMS temperatures. I. Variability and comparison with background winds, *J. Atmos. Sci.*, **51**, 2461-2483, 1994.
- Fritts, D. C., and L. Yuan, An analysis of gravity wave ducting in the atmosphere: Eckart’s resonances in thermal and Doppler ducts, *J. Geophys. Res.*, **94**(D15), 18455–18466, 1989.
- Fritts, D. C., B. P. Williams, C. Y. She, J. D. Vance, M. Rapp, F.-J. Lübken, A. Müllemann, F. J. Schmidlin, and R. A. Goldberg, Observations of extreme temperature and wind gradients near the summer mesopause during the MaCWAVE/MIDAS rocket campaign, *Geophys. Res. Lett.*, **31**, L24S06, doi:10.1029/2003GL019389, 2004.
- Ganapol, B. D., L. F. Johnson, C. A. Hlavka, D. L. Peterson, and B. Bond, LCM2: A coupled leaf/canopy radiative transfer model, *Rem. Sens. Envir.*, **70**, 153–166, 1999.
- *Ganapol, B. D., R. H. Picard, J. R. Winick, P. P. Wintersteiner, and S. Woolf, Incorporation of azimuthal dependence into the LCM2 coupled leaf/canopy reflectance model, *Proc. SPIE*, **4542**, 214-222, 2002.
- *Ganapol, B. D., R. H. Picard, P. P. Wintersteiner, S. Woolf, R. Furfaro, and J. R. Winick, Passive foliage penetration using radiative-transfer methods, *Proceedings Space-Based EO/IR Surveillance Technology Conference*, Air Force Research Laboratory, Kirtland AFB, N.Mex., May 2003.
- *Ganapol, B. D., R. H. Picard, and J. R. Winick, Detection of a linearly polarized signal through foliage, *Proc. 27th Annual Review of Atmospheric Transmission Models*, Air Force Research Laboratory, Hanscom AFB, Mass., June 2005.
- **Gardner, J. L., M. López-Puertas, M. G. Mlynczak, B. Funke, F. J. Martin-Torres, J. M. Russell III, S. M. Miller, R. D. Sharma, and J. R. Winick, Comparison of nighttime NO 5.3 μm emissions in the thermosphere measured by MIPAS and

SABER, *J. Geophys. Res.-Space*, 112, A10301, doi:10.1029/2006JA011984, 5 Oct 2007.

- Gille, J. C., and F. B. House, On the inversion of limb radiance measurements. I: Temperature and thickness, *J. Atmos. Sci.*, 28, 1427-1442, 1971.
- Goldberg, R. A., and D. C. Fritts, Introduction to special section: The MaCWAVE-MIDAS Program to Study the Polar Summer Mesosphere, *Geophys. Res. Lett.*, 31, L24S01, doi:10.1029/2004GL021789, 2004.
- Goldberg, R. A., D. C. Fritts, B. P. Williams, F.-J. Lübken, M. Rapp, W. Singer, R. Latteck, P. Hoffmann, A. Müllemann, G. Baumgarten, F. J. Schmidlin, C.-Y. She, and D. A. Krueger, The MaCWAVE/MIDAS rocket and ground-based measurements of polar summer dynamics: Overview and mean state structure, *Geophys. Res. Lett.*, 31, L24S02, doi:10.1029/2004GL019411, 2004.
- Gordley, L. L., B. T. Marshall, and D. A. Chu, LINEPAK: Algorithms for modeling spectral transmittance and radiance, *J. Quant. Spectrosc. Radiat. Transfer*, 52(5), 563–580, 1994.
- Gruninger, J. H., R. Sundberg, J. Duff, J. H. Brown, R. Sharma, and R. Sears, Modeling for atmospheric background radiance structures, *Proc. SPIE*, 2580, 1-16, 1995.
- Gruninger, J. H., J. Duff, J. H. Brown, and W. A. M. Blumberg, Radiation transport effects and the interpretation of infrared images of gravity waves and turbulence, *Proc. SPIE*, 3495, 122-135, 1998.
- Gruninger, J. H., J. Duff, H. Dothe, and J. Brown, Incorporation of gravity wave models into SAMM, Tech Rpt AFRL-VS-TR-2004-1146, 2004.
- Gruninger, J., J. W. Duff, and J. H. Brown, Contributions of the OH airglow to space object irradiance, *Proc. SPIE*, 6745, 1N-1 – 1N-9, 2007.
- Hagan, M. E., M. D. Burrage, J. M. Forbes, J. Hackney, W. J. Randel, and X. Zhang, GSWM-98: Results for migrating solar tides, *J. Geophys. Res.*, 104, 6813-6828, 1999.
- Huang, C.-S., M. C. Kelley, and D. L. Hysell, Nonlinear Rayleigh-Taylor instabilities, atmospheric gravity waves and equatorial spread F, *J. Geophys. Res.*, 98(A9), 15631–15642, 1993.
- Huang, C.-S., and M. C. Kelley, Nonlinear evolution of equatorial spread F 1. On the role of plasma instabilities and spatial resonance associated with gravity wave seeding, *J. Geophys. Res.*, 101(A1), 283–292, 1996a.
- Huang, C.-S., and M. C. Kelley, Nonlinear evolution of equatorial spread F 2. Gravity wave seeding of Rayleigh-Taylor instability, *J. Geophys. Res.*, 101(A1), 293–302, 1996b.
- Huang, C.-S., and M. C. Kelley, Nonlinear evolution of equatorial spread F 4. Gravity waves, velocity shear, and day-to-day variability, *J. Geophys. Res.*, 101(A11), 24521–24532, 1996c.

- Huang, T.Y., H. Hur, T.F. Tuan, X. Li, E.M. Dewan, and R.H. Picard, Sudden narrow temperature-inversion-layer formation in ALOHA-93 as a critical-layer-interaction phenomenon, *J. Geophys. Res.*, *103*, 6323–6332, 1998.
- **Huang, T.-Y., M. P. Hickey, T.-F. Tuan, E. M. Dewan, and R. H. Picard, Further investigations of a mesospheric inversion layer observed in the ALOHA-93 Campaign, *J. Geophys. Res.*, *107*(D19), 4408, doi:10.1029/2001JD001186, 15 Oct 2002.
- Hysell, D. L., M. C. Kelley, W. E. Swartz, and R. F. Woodman, Seeding and layering of equatorial spread f by gravity waves, *J. Geophys. Res.*, *95*(A10), 17253–17260, 1990.
- Kumer, J. B., A. T. Stair, Jr., N. Wheeler, K. D. Baker, and D. J. Baker, Evidence for an $\text{OH}(\text{v}) \rightarrow \text{N}_2(\text{v}) \rightarrow \text{CO}_2(\text{v}_3) \rightarrow \text{CO}_2 + \text{h}\nu(4.3\mu\text{m})$ mechanism for the 4.3- μm airglow, *J. Geophys. Res.*, *83*, 4743, 1978.
- Kutepov A. A., A. G. Feofilov, B. T. Marshall, L. L. Gordley, W. D. Pesnell, R. A. Goldberg, J. M. Russell III, SABER temperature observations in the summer polar mesosphere and lower thermosphere: Importance of accounting for the $\text{CO}_2 \text{ v } 2$ quanta V–V exchange, *Geophys. Res. Lett.*, *33*, L21809, doi:10.1029/2006GL026591, 2006.
- Lighthill, J., *Waves in Fluids*, Cambridge Univ. Press, 1978.
- Lindborg, E., Can the atmospheric kinetic energy be explained by two-dimensional turbulence?, *J. Fluid Mech.*, *388*, 259-288, 1999.
- Llewellyn, E.J., N. D. Lloyd, D. A. Degenstein, R. L. Gattinger, S. V. Petelina, A. E. Bourassa, J. T. Wiensz, E. V. Ivanov, I. C. McDade, B. H. Solheim, J. C. McConnell, C. S. Haley, C. von Savigny, C. E. Sioris, C. A. McLinden, E. Griffioen, J. Kaminski, W. F. J. Evans, E. Puckrin, K. Strong, V. Wehrle, R. H. Hum, D. J. W. Kendall, J. Matsushita, D. P. Murtagh, S. Brohede, J. Stegman, G. Witt, G. Barnes, W. F. Payne, L. Piché, K. Smith, G. Warshaw, D.-L. Deslauniers, P. Marchand, E. H. Richardson, R. A. King, I. Wevers, W. McCreath, E. Kyrölä, L. Oikarinen, G. W. Leppelmeier, H. Auvinen, G. Mégie, A. Hauchecorne, F. Lefèvre, J. de La Nöe, P. Ricaud, U. Frisk, F. Sjöberg, F. von Scheele, and L. Nordh, The OSIRIS instrument on the Odin spacecraft, *Can. J. Phys.*, *82*, 411-422, doi:10.1139/P04-005, 2004.
- López-Puertas, M., and F. W. Taylor, *Non-LTE Radiative Transfer in the Atmosphere*, World Scientific, Singapore, 2001.
- López-Puertas, M., R. Rodrigo, J. J. López-Moreno, and F. W. Taylor, A non-LTE radiative transfer model for infrared bands in the middle atmosphere. II. CO_2 (2.7 and 4.3 μm) and water vapor (6.3 μm) bands and $\text{N}_2(1)$ and $\text{O}_2(1)$ vibrational levels, *J. Atmos. Terr. Phys.*, *48*(8), 749–764, 1986.
- López-Puertas, M., P. P. Wintersteiner, R. H. Picard, J. R. Winick, and R. D. Sharma, Comparison of line-by-line and Curtis matrix calculations for the vibrational temperatures and radiative cooling of the CO_2 15 μm bands in the middle and upper atmosphere, *J. Quant. Spectrosc. Radiat. Transfer*, *32*, 409-423, 1994.

- **López-Puertas, M., M. García-Comas, B. Funke, R. H. Picard, J. R. Winick, P. P. Wintersteiner, M. G. Mlynczak, C. J. Mertens, J. M. Russell III, and L. L. Gordley, Evidence for an OH(v) excitation mechanism of CO₂ 4.3 μm nighttime emission from SABER/TIMED measurements, *J. Geophys. Res.*, *109*(D9), D09307, doi:10.1029/2003JD004383, 13 May 2004.
- *Loughmiller, P. J., M. C. Kelley, E. M. Dewan, F. J. Garcia, J. L. Makela, and S. Smith, Sharp mesospheric fronts: Dual bore theory and comparison to nonlinear numerical simulations, submitted for publication Apr 2006.
- *Loughmiller, P. J., M. C. Kelley, M. P. Hickey, R. H. Picard, P. P. Wintersteiner, J. R. Winick, and E. M. Dewan, Observational and modeling study of mesospheric bores, *Proceedings Advanced Maui Optical and Space Surveillance Technologies (AMOS) Technical Conference*, 2007.
- Lübken, F.-J., Thermal structure of the Arctic summer mesosphere, *J. Geophys. Res.*, *104*, 9135–9149, 1999.
- Lübken, F.-J., and U. von Zahn, Thermal structure of the mesopause region at polar latitudes, *J. Geophys. Res.*, *96*(D11), 20841–20857, 1991.
- Makhlouf, U. B., R. H. Picard, and J. R. Winick, A model for the response of the atomic oxygen 557.7nm and the OH Meinel airglow to atmospheric gravity waves in a realistic atmosphere, *J. Geophys. Res.*, *103*(D6), 6261–6269, 1998.
- Makhlouf, U. B., R. H. Picard, J. R. Winick, and T. F. Tuan, Photochemical-dynamical modeling of the measured response of airglow to gravity waves, *J. Geophys. Res.*, *100*(D6), 11289–11311, 1991.
- Marshall, B. T., L. L. Gordley, D. A. Chu, BANDPAK: Algorithms for modeling broadband transmission and radiance, *J. Quant. Spectrosc. Radiat. Transfer*, *52*(5), 581–599, 1994.
- McClure, J. P., S. Singh, D. K. Bamgboye, F. S. Johnson, and H. Kil, Occurrence of equatorial F region irregularities: Evidence for tropospheric seeding, *J. Geophys. Res.*, *103*(A12), 29119–29135, 1998.
- Melo, S. M. L., R. P. Lowe, and J. P. Russell, Double-peaked hydroxyl airglow profiles observed from WINDII/UARS, *J. Geophys. Res.*, *105*(D10), 12397–12403, 2000.
- Meriwether, J. W., and A. J. Gerrard, Mesosphere inversion layers and stratosphere temperature enhancements, *Rev. Geophys.*, *42*, RG3003, doi:10.1029/2003RG000133, 2004.
- **Mertens, C. J., M. G. Mlynczak, M. López-Puertas, P. P. Wintersteiner, R. H. Picard, J. R. Winick, L. L. Gordley, and J. M. Russell III, Retrieval of mesospheric and lower thermospheric kinetic temperature from measurements of CO₂ 15 μm Earth limb emission under non-LTE conditions, *Geophys. Res. Lett.*, *28*, 1391–1394, 1 Apr 2001.
- *Mertens, C. J., M. G. Mlynczak, M. López-Puertas, P. P. Wintersteiner, R. H. Picard, J. R. Winick, L. L. Gordley, and J. M. Russell III, Retrieval of kinetic temperature and carbon dioxide abundances from nonlocal thermodynamic equilibrium limb emission

- measurements made by the SABER experiment on the TIMED satellite, *Proc. SPIE*, 4882, 162-171, 2003.
- **Mertens, C. J., F. J. Schmidlin, R. A. Goldberg, E. E. Remsberg, W. D. Pesnell, J. M. Russell III, M. G. Mlynczak, M. López-Puertas, P. P. Wintersteiner, R. H. Picard, J. R. Winick, and L. L. Gordley, SABER observations of mesospheric temperatures and comparisons with falling sphere measurements taken during the 2002 summer MaCWAVE campaign, *Geophys. Res. Lett.*, 31, L03105, doi:10.1029/2003GL018605, 5 Feb 2004.
- **Mertens, C. J., J. C. Mast, J. R. Winick, J. M. Russell III, M. G. Mlynczak, and D. S. Evans, Ionospheric E-region response to solar-geomagnetic storms observed by TIMED/SABER and application to IRI storm-model development, *Adv. Space Res.*, 39, 715-728, 2007.
- Mill, J. D., R. R. O’Neil, S. Price, G. J. Romick, O. M. Uy, and E. M. Gaposchkin, G. C. Light, W. W. Moore, Jr., T. L. Murdock, and A. T. Stair, Jr., “Midcourse Space Experiment,” *J. Spacecraft and Rockets*, 31, 900-907, 1994.
- Miller, S. M., J. R. Winick, and H. E. Snell, Simultaneous retrievals of middle atmospheric temperature and trace gas species volume mixing ratios from Cryogenic Infrared Radiance Instrumentation for Shuttle (CIRRIS 1A), *J. Geophys. Res.*, 104, 18697-18714, 1999.
- **Miller, S. M., J. R. Winick, H. E. Snell, Non-LTE effect on retrieval of temperature from the CO₂ laser band using CIRRIS 1A data, *J. Geophys. Res.*, 105, 10193-10202, 2000.
- **Mlynczak, M.G., F. J. Martin-Torres, J. M. Russell, K. Beaumont, S. Jacobson, M. López-Puertas, B. Funke, C. Mertens, L. Gordley, R. H. Picard, J. R. Winick, P. P. Wintersteiner, L. Paxton, and J. Kozyra, The natural thermostat of nitric oxide emission at 5.3 μm in the thermosphere observed during the solar storms of April 2002, *Geophys. Res. Lett.*, 30, doi:10.1029/2003GL017693, 2003.
- **Mlynczak, M. G., F. J. Martin-Torres, J. M. Russell, K. Beaumont, S. Jacobson, M. López-Puertas, B. Funke, C. Mertens, L. Gordley, R. H. Picard, J. R. Winick, P. P. Wintersteiner, L. Paxton, and J. Kozyra, The natural thermostat of nitric oxide emission at 5.3 μm in the thermosphere observed during the solar storms of April 2002, *Geophys. Res. Lett.*, 30(21), 2100, doi:10.1029/2003GL017693, 7 Nov 2003.
- **Mlynczak, M. G., F. J. Martin-Torres, G. Crowley, D. P. Kratz, B. Funke, M. López-Puertas, J. M. Russell III, J. Kozyra, C. Mertens, R. Sharma, L. Gordley, R. Picard, J. Winick, L. Paxton, Energy transport in the thermosphere during the solar storms of April 2002, *J. Geophys. Res.*, 110, A12S25, doi:10.1029/2005JA011141, 15 Dec 2005.
- Monnier, J. D., Optical interferometry in astronomy, *Rep. Prog. Phys.*, 66, 789-857, 2003.
- Nebel, H., P. P. Wintersteiner, R. H. Picard, J. R. Winick, and R. D. Sharma, CO₂ non-local thermodynamic equilibrium radiative excitation and infrared dayglow at 4.3

- μm : Application to Spectral Infrared Rocket Experiment data, *J. Geophys. Res.*, **99**, 10409–10419, 1994.
- O’Neil, R. R., H. A. B. Gardiner, J. Gibson, C. Humphrey, R. Hegblom, M. E. Fraser, M. Kendra, P. Wintersteiner, and C. Rice, “Midcourse Space Experiment (MSX),” *Proc. Soc. Photo. Opt. Instrum. Eng.*, **2223** (25) 264-273, 1994.
- O’Neil, R. R., H. A. B. Gardiner, J. J. Gibson, and A. T. Stair, Midcourse Space Experiment (MSX): Overview of mid-wave infrared atmospheric gravity waves in earth limb and terrestrial backgrounds, *E-O Propagation, Signature and System Performance Under Adverse Meteorological Conditions Considering Out-of-Area Operations*, NATO, Research and Technology Organization Meeting Proceedings 1, RTO-MP-1, Sensors and Electronics Technology (SET) Panel, 1998.
- ** O’Neil, R. R., J. R. Winick, R. H. Picard, and M. Kendra, Auroral NO^+ $4.3\mu\text{m}$ emission observed from the Midcourse Space Experiment: Multi-platform observations of 9 February 1997, *J. Geophys. Res.-Space*, **112**, A06327, doi:10.1029/2006JA012120, 29 Jun 2007.
- Osborne, A. R., and T. L. Burch, Internal solitons in the Andaman Sea, *Science*, **208**, 451-460, 1980.
- Pandya, R. E., and M. J. Alexander, Linear stratospheric gravity waves above convective thermal forcing, *J. Atmos. Sci.*, **56**, 2434-2446, 1999.
- Pasko, V. P., Atmospheric physics: Electric jets, *Nature*, **423**, 927-929, 2003.
- Piani, C., D. Durran, M. J. Alexander, and J. R. Holton, A numerical study of three dimensional gravity waves triggered by deep tropical convection and their role in the dynamics of the QBO, *J. Atmos. Sci.*, **57**, 3689, 2000.
- Picard, R. H., J. R. Winick, R. D. Sharma, A. S. Zachor, P. J. Espy, and C. R. Harris, Interpretation of infrared measurements of the high-latitude thermosphere from a rocket-borne interferometer, *Adv. Space Res.*, **7**(10), 10-23 – 10-30, 1987.
- Picard R. H., R. R. O’Neil, H. A. Gardiner, J. Gibson, J. R. Winick, W. O. Gallery, A. T. Stair, Jr., P. P. Wintersteiner, E. R. Hegblom, and E. Richards, Remote sensing of discrete stratospheric gravity wave structure at $4.3\text{-}\mu\text{m}$ from the MSX satellite, *Geophys. Res. Lett.*, **25**, 2809-2812, 1998.
- *Picard, R. H., B. D. Ganapol, P. P. Wintersteiner, S. Woolf, and J. R. Winick, Passive radiative transfer of information through foliage canopies, *Proceedings 2001 MSS Specialty Groups on Passive Sensors; Camouflage, Concealment, and Deception; Detectors: and Materials*, Vol. 1, Infrared Information Analysis Center, Ann Arbor, Mich., Aug 2001.
- *Picard, R. H., J. R. Winick, and P. P. Wintersteiner, Nonequilibrium radiative transfer in structured atmospheres, *Proc. SPIE*, **4539**, 454-468, 2002.
- *Picard, R.H., E.M. Dewan, J.H. Brown, R.R. O’Neil, J.R. Winick, W.A.M. Blumberg, P.P. Wintersteiner, Structure of radiance from an atmosphere perturbed by superposed gravity waves, *Proc. SPIE*, **4882**, 149-161, 2003a.

- *Picard, R.H., coordinator; E. A. Bering, F. R. Chang Diaz, H. J. Christian, K. M. Groves, U. S. Inan, K. D. Papadopoulos, R. H. Picard, D. D. Sentman, E. M. Wescott, and E. R. Williams; *Potential for Discharge and Certain Other Space / Atmospheric Environment Effects in the Columbia Shuttle Orbiter Accident*; Report of Space / Atmospheric Environment Scientist Panel to Space Shuttle Vehicle Engineering Office, NASA/Johnson Space Center, AFRL, Hanscom AFB, Mass. (10 Jun 2003), 2003b.
- *Picard, R. H., P. P. Wintersteiner, J. R. Winick, C. J. Mertens, M. G. Mlynczak, J. M. Russell III, L. L. Gordley, W. E. Ward, C. Y. She, and R. R. O'Neil, Tidal and layer structure in the mesosphere and lower thermosphere from TIMED/SABER CO₂ 15- μ m emission, *Proc. SPIE*, 5571, 182-192, 2004a.
- *Picard, R.H., J. R. Winick, R. R. O'Neil, P. P. Wintersteiner, C. J. Mertens, M. G. Mlynczak, J. M. Russell III, L. L. Gordley, W. E. Ward, and C. Y. She, Tidal and layer structure in the mesosphere and lower thermosphere from TIMED/SABER CO₂ 15- μ m emission, Proceedings NASA TIMED Science Working Group (SWG) Meeting, SouthWest Research Institute, San Antonio, 2004b.
- Picone, J. M., A. E. Hedin, D. P. Drob, and A. C. Aikin, NRLMSISE-00 empirical model of the atmosphere: Statistical comparisons and scientific issues, *J. Geophys. Res.*, 107(A12), 1468, doi:10.1029/2002JA009430, 2002.
- Prakash, S., Production of electric field perturbations by gravity wave winds in the E region suitable for initiating equatorial spread F, *J. Geophys. Res.*, 104(A5), 10051–10069, 1999.
- Preusse, P., S. D. Eckermann, and D. Offermann, Comparison of global distributions of zonal mean gravity wave variance inferred from different satellite measurements, *Geophys. Res. Lett.*, 27, 3877-3880, 2000.
- Preusse, P., A. Dörnbrack, S. D. Eckermann, M. Riese, B. Schaeler, J. Bacmeister, D. Broutman, and K. U. Grossmann, Space based measurements of stratospheric mountain waves by CRISTA. 1. Sensitivity, analysis method and a case study, *J. Geophys. Res.*, 107, 8178, 2002.
- **Preusse, P., M. Ern, S. D. Eckermann, C. D. Warner, R. H. Picard, P. Knieling, J. Oberheide, M. Riese, J. M. Russell III, M. G. Mlynczak, and C. J. Mertens, Tropopause to mesopause gravity waves in August: Measurement and modeling, *J. Atm. Solar Terr. Phys.*, 68, 1730–1751, Oct 2006.
- Rapp, M., F.-J. Lübken, A. Müllemann, G. E. Thomas, and E. J. Jensen, Small-scale temperature variations in the vicinity of NLC: Experimental and model results, *J. Geophys. Res.*, 107(D19), 4392, doi:10.1029/2001JD001241, 2002.
- Reid, S. J., and G. Vaughan, Occurrence of ozone laminae near the boundary of the stratosphere polar vortex, *J. Geophys. Res.*, 98, 8883–8890, 1993.
- Richards, P. G., Ion and neutral density variations during ionospheric storms in September 1974: comparison of measurement and models, *J. Geophys. Res.*, 107(A11), 1361, doi:10.1029/2002JA00978, 2002.

- Roble, R. G., and E. C. Ridley, Thermosphere-Ionosphere-Mesosphere-Electro Dynamics General Circulation Model (TIME-GCM): Equinox solar cycle minimum simulations (300 – 500 km), *Geophys. Res. Lett.*, 22, 417, 1994.
- Rodgers, C. D., Retrieval of atmospheric temperature and composition from remote measurements of thermal radiation, *Rev. Geophys.*, 14, 609-624, 1976.
- Rodgers, C. D., *Inverse Methods for Atmospheric Sounding*, World Scientific, Singapore, 2000.
- Rothman, L. S., D. Jacquemart, A. Barbe, D. C. Benner, M. Birk, L. R. Brown, M. R. Carleer, C. Chackerian Jr., K. Chance, L. H. Coudert, V. Dana, V. M. Devi, J.-M. Flaud, R. R. Gamache, A. Goldman, J.-M. Hartmann, K. W. Jucks, A. G. Maki, J.-Y. Mandin, S. T. Massie, J. Orphal, A. Perrin, C. P. Rinsland, M. A. H. Smith, J. Tennyson, R. N. Tolchenov, R. A. Toth, J. Vander Auwera, P. Varanasi, and G. Wagner, The HITRAN 2004 molecular spectroscopic database, *J. Quant. Spectrosc. Radiat. Transfer*, 96, 139–204, 2005.
- Russell, J. M., III, M. G. Mlynczak, L. L. Gordley, J. Tansock, and R. Esplin, An overview of the SABER experiment and preliminary calibration results, *Proc. SPIE*, 3756, 277– 288, 1999.
- *Russell, J. M., III, M. G. Mlynczak, L. L. Gordley, C. J. Mertens, E. E. Remsberg, B. T. Marshall, G. Paxton, P. McMichael, J. G. Wells, M. Lopez-Puertas, M. García-Comas, R. H. Picard, B. Funke, P. P. Wintersteiner, J. R. Winick, D. Baker, G. Lingenfelter, and K. I. Beaumont, *SABER Experiment 2003 Annual Report*, Hampton Univ., Hampton, Va., 2004.
- *Schäfer, K. P., O. Lado-Bordowsky, A. Comeron, and R. H. Picard, eds., *Remote Sensing of Clouds and the Atmosphere VII*, SPIE, Bellingham, Wash., 2003 [*Proc. SPIE*, Vol. 4882].
- *Schäfer, K. P., A. Comerón, M. R. Carleer, and R. H. Picard, eds., *Remote Sensing of Clouds and the Atmosphere VIII*, SPIE, Bellingham, Wash., 2004a [*Proc. SPIE*, Vol. 5235].
- *Schäfer, K. P., A. Comerón, M. R. Carleer, R. H. Picard, and N. I. Sifakis, eds., *Remote Sensing of Clouds and the Atmosphere IX*, SPIE, Bellingham, Wash., 2004b [*Proc. SPIE*, Vol. 5571].
- *Schäfer, K. P., A. Comerón, J. R. Slusser, R. H. Picard, M. Carleer, and N. Sifakis, eds., *Remote Sensing of Clouds and the Atmosphere X*, SPIE, Bellingham, Wash., 2005 [*Proc. SPIE*, Vol. 5979].
- **Sentman, D. D., E. M. Wescott, R. H. Picard, J. R. Winick, H. C. Stenbaek-Nielsen, E. M. Dewan, D. R. Moudry, F. S. Sao Sabbas, and M. J. Heavner, Simultaneous observation of mesospheric gravity waves and sprites generated by a Midwestern thunderstorm, *J. Atmos. Solar Terr. Phys.*, 65, 537-550, Mar 2003 [Special Issue on Sprites, Elves and their Global Activities].
- **Sharma, R. D., R. O'Neil, H. Gardiner, J. Gibson, H. Dothe, J. W. Duff, P.P. Wintersteiner, and M. Kendra, Midcourse Space Experiment: Auroral enhancement

- of nitric oxide medium-wave infrared emission observed by Spatial Infrared Imaging Telescope III radiometer, *J. Geophys. Res.*, *106*, 21351-21365, 1 Oct 2001.
- **She, C. Y., T. Li, B. P. Williams, T. Yuan, and R. H. Picard, Concurrent OH imager and sodium temperature/wind lidar observation of a mesopause region undular bore event over Fort Collins/Platteville, CO, *J. Geophys. Res.*, *109*, D22107, doi:10.1029/2004JD004742, 27 Nov 2004.
- Siewert, C. E., J. R. Maiorino, and M. N. Ozisik, (1980), The use of the FN method for radiative transfer problems with reflective boundary conditions, *J. Quant. Spectrosc. Radiat. Transfer*, *23*, 565–573, 1980.
- Simpson, J. E., *Gravity Currents in the Environment and the Laboratory*, 2nd ed., Cambridge Univ. Press, 1997.
- Siskind, D. E., S. D. Eckermann, L. Coy, J. P. McCormack, and C. E. Randall, On recent interannual variability of the Arctic winter mesosphere: Implications for tracer descent, *Geophys. Res. Lett.*, *34*, L09806, doi:10.1029/2007GL029293, 2007.
- *Smith, D. R., R. D. Sharma, J. R. Winick, R. H. Picard, S. Miller, and J. Duff, Possible sources of unexplained auroral enhancements observed in SWIR OH filter passbands by the NASA SABER experiment during an intense geomagnetic storm, *Proceedings Space-Based EO/IR Surveillance Technology Conference*, Air Force Research Laboratory, Kirtland AFB, N.Mex., May 2003.
- Smith, H. J. P., D. J. Dube, M. E. Gardner, S. A. Clough, F. X. Kneizys, and L. S. Rothman, *FASCODE – Fast Atmospheric Signature Code (Spectral Transmittance and Radiance)*, Tech Rpt AFGL-TR-78-0081, Air Force Geophysics Laboratory, Hanscom AFB, Mass., 1978.
- Smith, R. K., Traveling waves and bores in the lower atmosphere: The "Morning Glory" and related phenomena, *Earth Sci. Rev.*, *25*, 267-290, 1988.
- Smith, S. A., D. C. Fritts, and T. E. Van Zandt, Evidence for a saturated spectrum of atmospheric gravity waves, *J. Atmos. Sci.*, *44*, 1404-1410, 1987.
- Stair, A. T., Jr., J. C. Ulwick, K. D. Baker, and D. J. Baker, Rocketborne observations of atmospheric infrared emissions in the auroral region, *Atmospheres of Earth and the Planets*, B. M. McCormac, ed., D. Reidel Publishing Co., Dordrecht, Netherlands, 1975.
- Stair, A. T., Jr., R. D. Sharma, R. M. Nadile, D. J. Baker, and W. F. Grieder, Observations of limb radiance with cryogenic Spectral Infrared Rocket Experiment, *J. Geophys. Res.*, *90*(A10), 9763–9775, 1985.
- Su, H. T., R. R. Hsu, A. B. Chen, Y. C. Wang, W. S. Hsiao, W. C. Lai, L. C. Lee, M. Sato, and H. Fukunishi, Gigantic jets between a thundercloud and the ionosphere, *Nature*, *423*, 974-976, 2003.
- Sundberg, R. L., J. W. Duff, J. H. Gruninger, L. S. Bernstein, M. W. Matthew, S. M. Adler-Golden, D. C. Robertson, R. D. Sharma, J. H. Brown, and R. J. Healey, SHARC, A model for calculating atmospheric infrared radiation under nonequilibrium conditions, *The upper mesosphere and lower thermosphere: A*

- review of experiment and theory*, Geophys. Monogr. Series, Vol. 87, pp. 287-295, American Geophysical Union, Washington, D.C., 1995.
- Tatarski, V. I., *The Effects of the Turbulent Atmosphere on Wave Propagation*, Rpt TT 68-50464, National Science Foundation, Washington, D.C., 1968.
- Taylor, M. J., and M. A. Hapgood, Identification of a thunderstorm as a source of short period gravity waves in the upper atmospheric nightglow emissions, *Planet Space Sci.*, 36, 975-985, 1988.
- Taylor, M. J., D. N. Turnbull, and R. P. Lowe, Spectrometric and imaging measurements of a spectacular gravity wave event observed during the ALOHA-93 Campaign, *Geophys. Res. Lett.*, 22, 2849, 1995.
- *Taylor, M. J., W. R. Pendleton, Jr., S. H. Seo, and R. H. Picard, Remote sensing of gravity wave intensity and temperature signatures at mesopause heights using the nightglow emissions, *Proc. SPIE*, 4882, 122-133, 2003.
- Vadas, S. L., and D. C. Fritts, Thermospheric responses to gravity waves arising from mesoscale convective complexes, *J. Atmos. Solar-Terr. Phys.*, 66, 781-804, 2004.
- Vanderbilt, V. C., L. Grant, and C. S. T. Daughtry, Polarization of light scattered by vegetation, *Proc. IEEE*, 73, 1012-1024, 1985a.
- Vanderbilt, V. C., L. Grant, L. L. Biehl, and B. F. Robinson, Specular, diffuse, and polarized light scattered by two wheat canopies, *Appl. Opt.*, 24, 2408-2418, 1985b.
- Wescott, E. M., D. D. Sentman, D. L. Osborne, D. L. Hampton, and M. J. Heavner, Preliminary results from the Sprites 94 aircraft campaign: 2. Blue jets, *Geophys. Res. Lett.*, 22, 1209-1212, 1995.
- Wescott, E. M., D. D. Sentman, M. J. Heavner, D. L. Hampton, and O. H. Vaughan, Blue starters: Brief upward discharges from an intense Arkansas thunderstorm, *Geophys. Res. Lett.*, 23, 2153-2156, 1996.
- Wescott, E. M., D. D. Sentman, M. J. Heavner, D. L. Hampton, and O. H. Vaughan, Blue jets: Their relationship to lightning and very large hailfall, and physical mechanisms for their production. *J. Atmos. Solar Terr. Phys.*, 60, 713-724, 1998.
- Winick, J. R., R. H. Picard, R. A. Joseph, R. D. Sharma, and P. P. Wintersteiner, An infrared spectral radiance code for the auroral thermosphere (AARC), AFRL-TR-87-0334, Air Force Geophysics Laboratory, Hanscom Air Force Base, Mass., 1987.
- *Winick, J. R., M. G. Mlynczak, P. P. Wintersteiner, F.-J. Martin-Torres, R. H. Picard, L. Paxton, M. López-Puertas, J. M. Russell III, A. Christensen, and L. L. Gordley, Thermospheric infrared radiance response to the April 2002 geomagnetic storm from SABER infrared and GUVI ultraviolet limb data, *Proc. SPIE*, 5235, 251-263, 2004a.
- *Winick, J. R., M. G. Mlynczak, P. P. Wintersteiner, F.-J. Martin-Torres, R. H. Picard, M. López-Puertas, J. M. Russell III, and L. Gordley, Thermospheric infrared emission response to major geomagnetic disturbances from SABER data: X-ray flare response, Proceedings NASA TIMED Science Working Group (SWG) Meeting, SouthWest Research Institute, San Antonio, 2004b.

- Wintersteiner, P.P., R.H. Picard, R.D. Sharma, J.R. Winick, and R.A. Joseph, Line-by-line radiative excitation model for the non-equilibrium atmosphere: Application to CO₂ 15- μ m emission, *J. Geophys. Res.*, 97, 18083–18117, 1992.
- *Wintersteiner, P. P., J. R. Winick, R. H. Picard, C. J. Mertens, M. G. Mlynczak, J. M. Russell III, and L. L. Gordley, Tidal influences on radiance structure in the mesosphere/lower thermosphere (MLT) region as seen in TIMED/SABER data, *Proc. 27th Annual Review of Atmospheric Transmission Models*, Air Force Research Laboratory, Lexington, Mass., June 2005.
- Wise, J. O., R. L. Carovillano, H. C. Carlson, R. G. Roble, S. Adler-Golden, R. M. Nadile, and M. Ahmadjian, CIRRIS 1A global observations of 15- μ m CO₂ and 5.3- μ m NO limb radiance in the lower thermosphere during moderate to active geomagnetic activity, *J. Geophys. Res.*, 100(A11), 21357–21373, 1995.
- Wu, D.L., Horizontal wavenumber spectra of MLS radiance fluctuations, *J. Atmos. Solar Terr. Phys.*, 63, 1465–1477, 2001.
- Yee, J. H., E. R. Talaat, A. B. Christensen, T. L. Killeen, J. M. Russell, T. N. Woods, TIMED instruments, *Johns Hopkins APL Technical Digest*, 24, 156–164, 2003.
- Zalevsky, Z., and D. Mendlovic, *Optical Superresolution*, Springer-Verlag, New York, 2004.

PUBLICATIONS - 2000-2007

****Refereed**

- E. M. Dewan** and **N. Grossbard**, Power spectral artifacts in published balloon data and implications regarding saturated gravity wave theories, *J. Geophys. Res.*, **105**, 4667-4683, 2000.
- E. M. Dewan** and **N. Grossbard**, The inertial range 'outer scale' and optical turbulence, *Envir. Fluid Mech*, **7**, 383-396, Oct 2007.
- E. M. Dewan** and **R. H. Picard**, On the origin of mesospheric bores, *J. Geophys. Res.*, **106**, 2921-2927, 16 Feb 2001.
- J. L. Gardner, M. López-Puertas, M. G. Mlynczak, B. Funke, F. J. Martin-Torres, J. M. Russell III, S. M. Miller, R. D. Sharma, and **J. R. Winick**, Comparison of nighttime NO 5.3 μm emissions in the thermosphere measured by MIPAS and SABER, *J. Geophys. Res.-Space*, **112**, A10301, doi:10.1029/2006JA011984, 5 Oct 2007.
- T.-Y. Huang, M. P. Hickey, T.-F. Tuan, **E. M. Dewan**, and **R. H. Picard**, Further investigations of a mesospheric inversion layer observed in the ALOHA-93 Campaign, *J. Geophys. Res.*, **107**(D19), 4408, doi:10.1029/2001JD001186, 15 Oct 2002.
- M. López-Puertas, M. García-Comas, B. Funke, **R. H. Picard**, **J. R. Winick**, **P. P. Wintersteiner**, M. G. Mlynczak, C. J. Mertens, J. M. Russell III, and L. L. Gordley, Evidence for an OH(v) excitation mechanism of CO₂ 4.3 μm nighttime emission from SABER/TIMED measurements, *J. Geophys. Res.*, **109**, D09307, doi:10.1029/2003JD004383, 13 May 2004.
- Lübken, F.-J., and U. von Zahn, Thermal structure of the mesopause region at polar latitudes, *J. Geophys. Res.*, **96**, 20841-20857, 1991.
- C. J. Mertens, M. G. Mlynczak, M. López-Puertas, **P.P. Wintersteiner**, **R. H. Picard**, **J. R. Winick**, L. L. Gordley, and J. M. Russell III, Retrieval of mesospheric and lower thermospheric kinetic temperature from measurements of CO₂ 15 μm Earth limb emission under non-LTE conditions, *Geophys. Res. Lett.*, **28**, 1391-1394, 1 Apr 2001.
- C. J. Mertens, F. J. Schmidlin, R. A. Goldberg, E. E. Remsberg, W. D. Pesnell, J. M. Russell III, M. G. Mlynczak, M. López-Puertas, **P. P. Wintersteiner**, **R. H. Picard**, **J. R. Winick**, and L. L. Gordley, SABER observations of mesospheric temperatures and comparisons with falling sphere measurements taken during the 2002 summer MacWAVE campaign, *Geophys. Res. Lett.*, **31**, L03105, doi:10.1029/2003GL018605, 5 Feb 2004.

- C. J. Mertens, J. C. Mast, **J. R. Winick**, J. M. Russell III, M. G. Mlynczak, and D. S. Evans, Ionospheric E-region response to solar-geomagnetic storms observed by TIMED/SABER and application to IRI storm-model development, *Adv. Space Res.*, **39**, 715-728, 2007.
- S. M. Miller, **J. R. Winick**, H. E. Snell, Non-LTE effect on retrieval of temperature from the CO₂ laser band using CIRRIS 1A data, *J. Geophys. Res.*, **105**, 10193-10202, 2000.
- M. G. Mlynczak, F. J. Martin-Torres, J. M. Russell, K. Beaumont, S. Jacobson, M. López-Puertas, B. Funke, C. Mertens, L. Gordley, **R. H. Picard**, **J. R. Winick**, **P. P. Wintersteiner**, L. Paxton, and J. Kozyra, The natural thermostat of nitric oxide emission at 5.3 μm in the thermosphere observed during the solar storms of April 2002, *Geophys. Res. Lett.*, **30**(21), 2100, doi:10.1029/2003GL017693, 7 Nov 2003.
- M. G. Mlynczak, F. J. Martin-Torres, G. Crowley, D. P. Kratz, B. Funke, M. López-Puertas, J. M. Russell III, J. Kozyra, C. Mertens, R. Sharma, L. Gordley, **R. Picard**, **J. Winick**, L. Paxton, Energy transport in the thermosphere during the solar storms of April 2002, *J. Geophys. Res.*, **110**, A12S25, doi:10.1029/2005JA011141, 15 Dec 2005.
- R. R. O'Neil**, **J. R. Winick**, **R. H. Picard**, and M. Kendra, Auroral NO⁺ 4.3 μm emission observed from the Midcourse Space Experiment: Multi-platform observations of 9 February 1997, *J. Geophys. Res.-Space*, **112**, A06327, doi:10.1029/2006JA012120, 29 Jun 2007.
- P. Preusse, M. Ern, S. D. Eckermann, C. D. Warner, **R. H. Picard**, P. Knieling, J. Oberheide, M. Riese, J. M. Russell III, M. G. Mlynczak, and C. J. Mertens, Tropopause to mesopause gravity waves in August: Measurement and modeling, *J. Atmos. Solar Terr. Phys.*, **68**, 1730–1751, Oct 2006.
- D. D. Sentman, E. M. Wescott, **R. H. Picard**, **J. R. Winick**, H. C. Stenbaek-Nielsen, **E. M. Dewan**, D. R. Moudry, F. S. Sao Sabbas, and M. J. Heavner, Simultaneous observation of mesospheric gravity waves and sprites generated by a Midwestern thunderstorm, *J. Atmos. Solar Terr. Phys.*, **65**, 537-550, Mar 2003 [Special Issue on Sprites, Elves and their Global Activities].
- R. D. Sharma, **R. O'Neil**, H. Gardiner, J. Gibson, H. Dothe, J. W. Duff, **P.P. Wintersteiner**, and M. Kendra, Midcourse Space Experiment: Auroral enhancement of nitric oxide medium-wave infrared emission observed by Spatial Infrared Imaging Telescope III radiometer, *J. Geophys. Res.*, **106**, 21351-21365, 1 Oct 2001.
- C. Y. She, T. Li, B. P. Williams, T. Yuan, and **R. H. Picard**, Concurrent OH imager and sodium temperature/wind lidar observation of a mesopause region undular bore event over Fort Collins/Platteville, CO, *J. Geophys. Res.*, **109**, D22107, doi:10.1029/2004JD004742, 27 Nov 2004.

***Unrefereed**

- J. H. Brown, **R. R. O'Neil**, **R. H. Picard**, W. A. M. Blumberg, E. M. Dewan, N. A. Grossbard, and J. H. Gruninger, Structure in middle and upper atmospheric infrared radiance, *Proc. SPIE*, 4539, 431-445, 2002.
- A. Comerón, **R. H. Picard**, K. P. Schäfer, J. R. Slusser, and A. Amodeo, eds., *Remote Sensing of Clouds and the Atmosphere XII*, SPIE, Bellingham, Wash., 2007 [*Proc. SPIE*, Vol. 6745].
- E. M. Dewan**, *An Experimental Test to Compare Viability of Various Theories of Atmospheric Velocity Fluctuations*, Report AFRL-VS-TR-2001-1618, Air Force Research Laboratory, Hanscom AFB, Mass., 2001.
- E. M. Dewan**, Optical turbulence forecasting, *Proceedings Advanced Maui Optical and Space Surveillance Technologies (AMOS) Technical Conference*, 2003.
- E. M. Dewan**, Modeling and forecasting atmospheric optical turbulence, *Technology Horizons*, AFRL, Aug 2004.
- E. M. Dewan** and **N. Grossbard**, Intermittence in stratospheric gravity wave cascades, submitted for publication (May 2007), 2007.
- D. E. Donatelli, J. H. Brown, E. M. Dewan, J. J. Gibson, K. E. Kraemer, **R. R. O'Neil**, **R. H. Picard**, S. D. Price, R. D. Sharma, and **J. R. Winick**, *Background Clutter Specification and Mitigation*, Report AFRL-VS-HA-TR-2005-1107, Air Force Research Laboratory, Hanscom AFB, Mass. [limited distribution, U.S. Govt. and contractors], 29 Jul 2005.
- B. D. Ganapol, **R. H. Picard**, **J. R. Winick**, **P. P. Wintersteiner**, and S. Woolf, Incorporation of azimuthal dependence into the LCM2 coupled leaf/canopy reflectance model, *Proc. SPIE*, 4542, 214-222, 2002.
- B. D. Ganapol, **R. H. Picard**, **P. P. Wintersteiner**, S. Woolf, R. Furfaro, and **J. R. Winick**, Passive foliage penetration using radiative-transfer methods, *Proceedings Space-Based EO/IR Surveillance Technology Conference*, Air Force Research Laboratory, Kirtland AFB, N.Mex., May 2003.
- B. D. Ganapol, **R. H. Picard**, and **J. R. Winick**, Detection of a linearly polarized signal through foliage, *Proc. 27th Annual Review of Atmospheric Transmission Models*, Air Force Research Laboratory, Lexington, Mass., June 2005.
- P. J. Loughmiller, M. C. Kelley, **E. M. Dewan**, F. J. Garcia, J. L. Makela, and S. Smith, Sharp mesospheric fronts: Dual bore theory and comparison to nonlinear numerical simulations, submitted for publication Apr 2006.
- P. J. Loughmiller, M. C. Kelley, M. P. Hickey, **R. H. Picard**, **P. P. Wintersteiner**, **J. R. Winick**, and **E. M. Dewan**, Observational and modeling study of mesospheric bores, *Proceedings Advanced Maui Optical and Space Surveillance Technologies (AMOS) Technical Conference*, 2007.
- C. J. Mertens, M. G. Mlynczak, M. López-Puertas, **P. P. Wintersteiner**, **R. H. Picard**, **J. R. Winick**, L. L. Gordley, and J. M. Russell III, Retrieval of kinetic temperature and

carbon dioxide abundances from nonlocal thermodynamic equilibrium limb emission measurements made by the SABER experiment on the TIMED satellite, *Proc. SPIE*, 4882, 162-171, 2003.

- R. H. Picard**, B. D. Ganapol, **P. P. Wintersteiner**, S. Woolf, and **J. R. Winick**, Passive radiative transfer of information through foliage canopies, *Proceedings 2001 MSS Specialty Groups on Passive Sensors; Camouflage, Concealment, and Deception; Detectors; and Materials*, Vol. 1, Infrared Information Analysis Center, Ann Arbor, Mich., Aug 2001.
- R. H. Picard**, **J. R. Winick**, and **P. P. Wintersteiner**, Nonequilibrium radiative transfer in structured atmospheres, *Proc. SPIE*, 4539, 454-468, 2002.
- R. H. Picard**, **E. M. Dewan**, J. H. Brown, **R. R. O'Neil**, **J. R. Winick**, W. A. M. Blumberg, **P. P. Wintersteiner**, Structure of radiance from an atmosphere perturbed by superposed gravity waves, *Proc. SPIE*, 4882, 149-161, 2003a.
- R. H. Picard**, coordinator; E. A. Bering, F. R. Chang Diaz, H. J. Christian, K. M. Groves, U. S. Inan, K. D. Papadopoulos, **R. H. Picard**, D. D. Sentman, E. M. Wescott, and E. R. Williams; *Potential for Discharge and Certain Other Space / Atmospheric Environment Effects in the Columbia Shuttle Orbiter Accident*; Report of Space / Atmospheric Environment Scientist Panel to Space Shuttle Vehicle Engineering Office, NASA/Johnson Space Center, AFRL, Hanscom AFB, Mass., 10 Jun 2003 (2003b).
- R. H. Picard**, **P. P. Wintersteiner**, **J. R. Winick**, C. J. Mertens, M.G. Mlynczak, J.M. Russell III, L. L. Gordley, W. E. Ward, C. Y. She, and **R. R. O'Neil**, Tidal and layer structure in the mesosphere and lower thermosphere from TIMED/SABER CO₂ 15- μ m emission, *Proc. SPIE*, 5571, 182-192, 2004.
- R.H. Picard**, **J. R. Winick**, **R. R. O'Neil**, **P. P. Wintersteiner**, C. J. Mertens, M. G. Mlynczak, J. M. Russell III, L. L. Gordley, W. E. Ward, and C. Y. She, Tidal and layer structure in the mesosphere and lower thermosphere from TIMED/SABER CO₂ 15- μ m emission, Proceedings NASA TIMED Science Working Group (SWG) Meeting, SouthWest Research Institute, San Antonio, Sep-Oct 2004.
- J. M. Russell III, M. G. Mlynczak, L. L. Gordley, C. J. Mertens, E. E. Remsberg, B. T. Marshall, G. Paxton, P. McNicholl, J. G. Wells, M. Lopez-Puertas, M. García-Comas, **R. H. Picard**, B. Funke, **P. P. Wintersteiner**, **J. R. Winick**, D. Baker, G. Lingenfelser, and K. I. Beaumont, *SABER Experiment 2003 Annual Report*, Hampton Univ., Hampton, Va., 2004.
- K. P. Schäfer, O. Lado-Bordowsky, A. Comeron, and **R. H. Picard**, eds., *Remote Sensing of Clouds and the Atmosphere VII*, SPIE, Bellingham, Wash., 2003 [*Proc. SPIE*, Vol. 4882].
- K. P. Schäfer, A. Comerón, M. R. Carleer, and **R. H. Picard**, eds., *Remote Sensing of Clouds and the Atmosphere VIII*, SPIE, Bellingham, Wash., 2004 [*Proc. SPIE*, Vol. 5235].

- K. P. Schäfer, A. Comerón, M. R. Carleer, **R. H. Picard**, and N. I. Sifakis, eds., *Remote Sensing of Clouds and the Atmosphere IX*, SPIE, Bellingham, Wash., 2004 [*Proc. SPIE*, Vol. 5571].
- K. P. Schäfer, A. Comerón, J. R. Slusser, **R. H. Picard**, M. Carleer, and N. Sifakis, eds., *Remote Sensing of Clouds and the Atmosphere X*, SPIE, Bellingham, Wash., 2005 [*Proc. SPIE*, Vol. 5979].
- D. R. Smith, R. D. Sharma, **J. R. Winick**, **R. H. Picard**, S. Miller, and J. Duff, Possible sources of unexplained auroral enhancements observed in SWIR OH filter passbands by the NASA SABER experiment during an intense geomagnetic storm, *Proceedings Space-Based EO/IR Surveillance Technology Conference*, Air Force Research Laboratory, Kirtland AFB, N.Mex., May 2003.
- M. J. Taylor, W. R. Pendleton, Jr., S. H. Seo, and **R. H. Picard**, Remote sensing of gravity wave intensity and temperature signatures at mesopause heights using the nightglow emissions, *Proc. SPIE*, 4882, 122-133, 2003.
- J. R. Winick**, **R. H. Picard**, **P. P. Wintersteiner**, M. G. Mlynczak, J. M. Russell III, and L. Gordley, SABER instrument on the NASA TIMED satellite: An overview and use of SABER data in Air Force infrared background models, *Proceedings Space-Based EO/IR Surveillance Technology Conference*, Air Force Research Laboratory, Kirtland AFB, N.Mex., May 2003.
- J. R. Winick**, **R. H. Picard**, M. G. Mlynczak, **P. P. Wintersteiner**, F.-J. Martin-Torres, L. J. Paxton, M. López-Puertas, J. M. Russell III, A. B. Christensen, and L. Gordley, Thermospheric infrared radiance response to the April 2002 geomagnetic storm from SABER infrared and GUVI ultraviolet limb data, *Proc. SPIE*, 5235, 250-263, 2004.
- J. R. Winick**, M. G. Mlynczak, **P. P. Wintersteiner**, F.-J. Martin-Torres, **R. H. Picard**, M. López-Puertas, J. M. Russell III, and L. Gordley, Thermospheric infrared emission response to major geomagnetic disturbances from SABER data: X-ray flare response, *Proceedings NASA TIMED Science Working Group (SWG) Meeting*, SouthWest Research Institute, San Antonio, Sep-Oct 2004.
- P. P. Wintersteiner**, **J. R. Winick**, **R. H. Picard**, C. J. Mertens, M. G. Mlynczak, J. M. Russell III, L. L. Gordley, Tidal influences on radiance structure in the mesosphere/lower thermosphere (MLT) region as seen in TIMED/SABER data, *Proc. 27th Annual Review of Atmospheric Transmission Models*, Air Force Research Laboratory, Lexington, Mass., June 2005.

LIST OF ACRONYMS AND ABBREVIATIONS

AARC	Auroral Atmospheric Radiance Code
ABL	AirBorne Laser
AF	Air Force
AFB	Air Force Base
AFOSR	Air Force Office of Scientific Research
AFRL	Air Force Research Laboratory
ALOHA	Airborne Lidar and Observations of the Hawaiian Airglow
AMOS	Air Force Maui Optical and Supercomputing Site
ARC	Atmospheric Radiance Code
ASPEN	Advanced SPace ENvironment (version of TIME-GCM code)
ATH	Above-the-horizon
BANDPAK	(Subroutine library for broadband atmospheric radiative transfer)
BDO	Benjamin-Davis-Ono (nonlinear wave equation)
BTH	Below-the-horizon
BV	Brunt-Vaisälä (BV frequency = frequency of buoyancy oscillations)
CARI	Cornell All-sky Roving Imager
CARMA	Community Aerosol and Radiation Model for Atmospheres
CASI	Cornell All-Sky Imager
CCD	Charge-coupled device
CF	Contribution function
CIRRIS	Cryogenic InfraRed Radiance Instrumentation for Shuttle
C/NOFS	Communication / Navigation Outage Forecasting System
CO ₂	Carbon dioxide
CRISTA	Cryogenic Infrared Spectrometers and Telescopes for the Atmosphere
CSU	Colorado State University
DNS	Direct numerical simulation
DoD	Department of Defense
DT	Diurnal tide
EOS	Earth Observing System
ESA	European Space Agency
ESF	Equatorial Spread-F
ENVISAT	ENVironmental SATellite
FASCODE	Fast Atmospheric Signature CODE
FAST	Fast Auroral SnapshoT Explorer
FLIP	Field-Line Interhemispheric Plasma (model)
FOV	Field-of-view
GATS	G&A Technical Software
GSWM	Global Scale Wave Model

GUVI	Global UltraViolet Imager
GW	Gravity (or buoyancy) wave
HAA	High-Altitude Airship
HALOE	HALogen Occultation Experiment
HITRAN	High-resolution TRANsmission molecular absorption database
IAA	Instituto de Astrofísica de Andalucía
IBC	International Brightness Coefficient – index for visible aurora
ICECAP	Infrared Chemistry Experiments - Coordinated Auroral Program
IR	Infrared
IRI	International Reference Ionosphere
JPL	Jet Propulsion Laboratory
KdV	Korteweg-deVries (nonlinear wave equation)
Kp	Planetary K-index (3-hour, measure of horizontal magnetometer fluctuations)
LaRC	Langley Research Center
LBH	Lyman-Birge-Hopfield (band system)
LBL	Line-by-line
LCM	Leaf Canopy Model
LINEPAK	(Subroutine library for high-resolution atmospheric radiative transfer)
LOS	Line-of-sight
LT	Local time
LTE	Local thermodynamic equilibrium
LWIR	Long-wave infrared
L ₀	Outer scale
MaCWAVE	Mountain and Convective Wave Ascending Vertically
MALT	Mesosphere and Lower Thermosphere (program, as in Maui-MALT)
MCC	Mesoscale Convective Complex
MIDEX	MID-size EXplorer
MAPSTAR	Middle Atmosphere Periodic Structure Associated Radiance
MDA	Missile Defense Agency
MIPAS	Michelson Interferometer for Passive Atmospheric Sensing
MLS	Microwave Limb Sounder
MLT	Mesosphere and Lower Thermosphere
MODTRAN	MODerate-resolution TRANsmittance code
MSIS	Mass Spectrometer, Incoherent Scatter radar model
MSSS	Maui Space Surveillance Station
MSX	Midcourse Space Experiment
MWIR	Mid-wave infrared

NASA	National Aeronautics and Space Administration
NE	Physics and Electronics Directorate, AFOSR
NIR	Near IR
NO	Nitric oxide
NRLMSISE	Naval Research Laboratory Mass Spectrometer, Incoherent Scatter radar, Extended model
NSF	National Science Foundation
NWT	Nonlinear wave theory
OH	Hydroxyl radical
OI	Atomic oxygen (neutral)
OSC	Optical Signatures Code
OSIRIS	Optical Spectrograph and InfraRed Imaging System
PI	Principal investigator
PSD	Power spectral density
Ri	Richardson number
RSO	Resident space object
RVB	AFRL, Space Vehicles Directorate, Battlespace Environment Division
SABER	Sounding of the Atmosphere using Broadband Emission Radiometry
SAG	SHARC Atmosphere Generator
SAMM	SHARC And MODTRAN Merged
SDT	Semidiurnal tide
SFFP	Summer Faculty Fellowship Program
SHARC	Strategic High-Altitude Radiance Code
SOAR	Structured Optical Atmospheric Radiance
SOI	Space object Identification
SPIM	SPEctral IMager
SPIRE	SPEctral Infrared Rocket Experiment
SPIRIT	SPEctral (or SPace) InfraRed Imaging Telescope,
SSA	Space Situational Awareness
SSGM	Strategic Scene Generator Model
SWIR	Short-Wave IR
TG	Taylor-Goldstein (equation)
TI	Temperature inversion
TIDI	TIMED Imaging Doppler Interferometer
TIMED	Thermosphere Ionosphere Mesosphere Energetics and Dynamics
TIME-GCM	Thermosphere Ionosphere Mesosphere Electrodynamic - General Circulation Model
TOC	Top-of-canopy
T _k	Kinetic temperature
T _{vib}	Vibrational temperature

UARS	Upper Atmosphere Research Satellite
UT	Universal time
UVISI	Ultraviolet and Visible Imagers and Spectrographic Imagers
VER	Volume emission rate
VIS	Visible
vmr	Volume mixing ratio
V-V	Vibration-to-vibration (transfer)
WINDII	Wind Imaging Interferometer